Mass Transport in PEM Water Electrolysers: A Review

M. Maier[a], K. Smith[a], J. Dodwell[a], G. Hinds[b], P.R. Shearing[a], D.J.L. Brett[a *]

[a] *Electrochemical Innovation Lab, Department of Chemical Engineering, UCL, London, WC1E 7JE, United Kingdom*

[b] *National Physical Laboratory, Hampton Road, Teddington, Middlesex, TW11 0LW, UK*

[*] *Corresponding author. Tel.: +44 (0)20 7679 3310; fax: +44 (0)20 7383 2348. E-mail address: d.brett@ucl.ac.uk (D.J.L. Brett).*

Abstract

While hydrogen generation by alkaline water electrolysis is a well-established, mature technology and currently the lowest capital cost electrolyser option; polymer electrolyte membrane water electrolysers (PEMWEs) have made major advances in terms of cost, efficiency, and durability, and the installed capacity is growing rapidly. This makes the technology a promising candidate for large-scale hydrogen production, and especially for energy storage in conjunction with renewable energy sources – an application for which PEMWEs offer inherent advantages over alkaline electrolysis. Improvements in PEMWE technology have led to increasingly high operational current densities, which requires adequate mass transport strategies to ensure sufficient supply of reactant and removal of products. This review discusses the current knowledge related to mass transport and its characterisation/diagnosis for PEMWEs, considering the flow channels, liquid-gas diffusion layer, and polymer electrolyte membrane in particular.

Keywords: PEM Water Electrolyser; Mass Transport; Flow Channels; Liquid-Gas Diffusion Layer; Two-Phase Flow

Contents

1 Introduction

The 'Hydrogen Economy' concept was developed in response to the world's rising energy consumption and concerns about pollution in the early 1970s [1]; with heightened awareness around climate change, the idea has gained increasing traction and has been discussed extensively [1–4]. The Hydrogen Economy is based on the use of hydrogen as a universal energy carrier (vector) and fuel. Transporting energy in the form of hydrogen through pipelines is more cost-efficient than the transport of electricity through wires [1]. Hydrogen is highly flexible and can be used in fuel cells to produce electricity or directly as a fuel in combustion engines [4].

The main drawback of this vision is the fact that hydrogen is rarely found naturally in its molecular H_2 form, but in other molecules such as water, crude oil or natural gas. This makes hydrogen production technologies the backbone of the Hydrogen Economy and a crucial bottle-neck for its realisation. The most commonly used methods of hydrogen production are reforming of hydrocarbons, the use of biomass in some form and water splitting [5,6]. Reforming and biomass gasification emit carbon dioxide as a by-product, which necessitates carbon capture and storage technology [5]. Hence, water electrolysis using electricity from renewable energy sources is an attractive alternative as its only local by-product is oxygen, when renewable electricity is used. Life cycle assessment analysing the whole supply chain yields a global warming potential for PEMWE hydrogen production of more than 30 $\frac{\mathrm{kg\ CO_2}}{\mathrm{kg\ H_2}}$ for the use of grid energy, and between 1 $\frac{\mathrm{kg\ CO_2}}{\mathrm{kg\ H_2}}$ and 3 $\frac{\mathrm{kg\ CO_2}}{\mathrm{kg\ H_2}}$ for a range of renewable energy sources [7], which compares to 4 $\frac{\mathrm{kg\ CO_2}}{\mathrm{kg\ H_2}}$ for biomass conversion and around 9 $\frac{\mathrm{kg\ CO_2}}{\mathrm{kg\ H_2}}$ for fossil fuel reforming [8].

The most widely applied and commercially viable water-splitting technology is alkaline electrolysis, which is mature and enables multimegawatt hydrogen production. Its advantages include simple design and a cheap electrolyte (KOH) [9]. However, alkaline electrolysis suffers from drawbacks such as relatively low current densities typically below 0.6 A cm^{-2} [10], resulting in a non-compact build, and a high gas crossover between anode and cathode [11].

In response to these disadvantages, polymer electrolyte membrane (PEM) water electrolysers have been developed, which use a polymer (ionomer) membrane instead of a liquid electrolyte to allow for transport of hydrogen ions. PEM water electrolysers (PEMWEs) can achieve high current densities of up to 10.0 A cm^{-2} [12], but are mostly used up to around 2.0 A cm^{-2} [10]. This, and the use of a thin membrane, allows for a very compact design and a significantly reduced gas crossover compared to alkaline electrolysis. In spite of these conceptual advantages, PEMWEs have only recently been commercialised; however, significant advances in deployment have been made in recent years, with plants being rated up to 6 MW [13], a 10 MW plant in installation [14], and a planned 100 MW plant [14]. Nevertheless, PEMWE has yet to be developed to the same scale of hydrogen production as alkaline electrolysis [10] and capital expenditure for PEMWE is still high, but is expected to reach cost parity with alkaline electrolysis by 2030 [15].

As most renewable energy technologies are intrinsically intermittent, stabilisation will be necessary to build a grid dominated by renewables. Among several potential solutions, such as Li-ion batteries and redox flow batteries, PEMWEs are a well-suited technology to provide this stabilisation in combination with PEM fuel cells. In the case of electricity overproduction, hydrogen can be produced and stored. When, at a later point, electricity production is not sufficient, the previously produced hydrogen can be converted into power using fuel cell technology. As a result, peaks and troughs in renewable electricity production are mitigated and the grid stabilized [10,16]. As electricity production from renewable sources is enforced by policy and growing exponentially worldwide, the need for an efficient and robust grid-scale storage system is increasing in tandem. PEMWEs are a prime candidate, especially with investment costs dropping [17], which makes the large-scale storage and intermittence control of renewable energy through hydrogen production and storage a more viable option.

As PEMWE technology matures, ever higher operational current densities are achieved. Increasing current density requires greater oxygen and hydrogen removal and access of water to the reaction sites, which need to be efficiently transported through the PEMWE. Mass transport is especially important at the anode, where water must be transported to the catalyst layer and simultaneously

oxygen needs to be transferred in concurrent flow from the reaction sites towards the flow channels. Given the increasing need and ability to operate at high current density the scientific literature dedicated to improving mass transfer in PEMWEs is expanding rapidly. This review examines this body of literature, providing an overview of the state of research and technology in relation to mass transport in PEMWEs and available diagnostic techniques used to analyse it, improve device design and operational conditions. This work focuses on the processes on the anode side and membrane; however, the mass transport on the cathode of a PEMWE can be mostly described analogously.

2 PEMWE Assembly

Figure 1 shows the assembly of a typical PEMWE with the catalyst coated membrane (CCM), the liquid-gas diffusion layer (LGDL) at the anode, the gas diffusion layer at the cathode (GDL), flow-fields, and end-plates. Gaskets (not displayed) are usually employed to keep LGDL, GDL, and CCM in place and to prevent leakage. The use of a CCM is the most commonly used approach, but it is possible to apply the catalysts to the surface of the LGDL/GDL and combine these with an uncoated ionomer membrane. This yields an equivalent sequence of functional layers and has been shown to produce comparable performance [18,19].

The single-cell PEMWE (Figure 1 (a)) shown here is typically used for research work and is well-suited to demonstrate the basic processes and function of a PEMWE. However, for commercial application PEMWE stacks are used, which combine multiple single cells into one unit [20], but are subject to the same processes discussed in this work.

Water enters the PEMWE through the end-plate on the anode side and is transported across the active area along the channels of the flow-field. Within the temperature range PEMWEs are typically operated the water is liquid. The water then crosses through the porous LGDL towards the anode catalyst layer (CL), where it is oxidised to form protons, electrons and oxygen. The protons are transported through the membrane to the cathode CL, where hydrogen is formed. However, the oxygen has to be transported from the anode CL, through the LGDL, back to the flow channels where

it is carried out of the PEMWE cell with the unreacted water. While crossing the LGDL, the oxygen gas is in counter-current flow to the water traveling from the flow-field to the catalyst layer. Even though it is not strictly necessary for the operation of a PEMWE, water can be circulated through the cathode side as well to facilitate hydrogen removal and ensure sufficient hydration of the membrane (shown in Figure 1 (b)); however, many PEMWE systems, in particular commercial plants, operate without water circulation at the cathode.

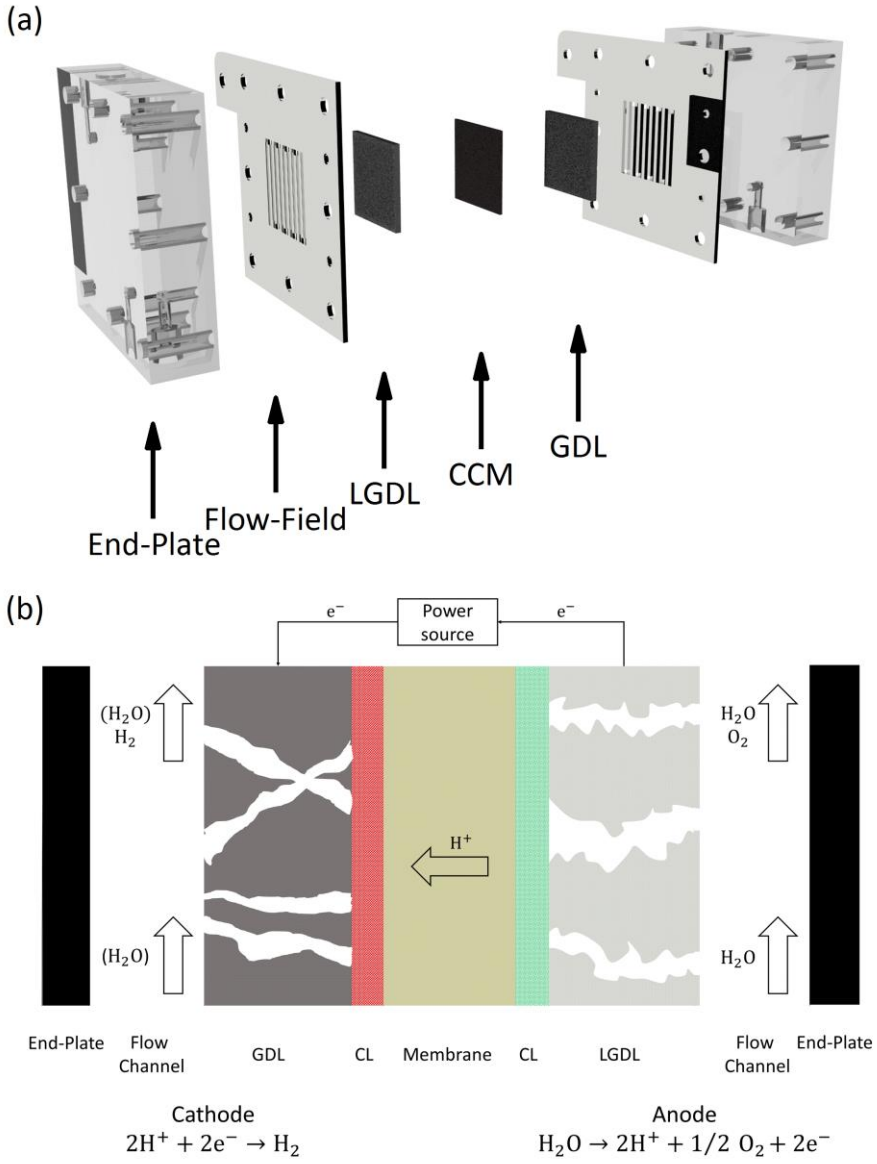

Fig. 1: (a) The assembly of a single-cell PEMWE with end-plates, flow-field, liquid-gas diffusion layer (LGDL), gas diffusion layer (GDL), and catalyst coated membrane (CCM). **(b)** Schematic of components and mass flows in a PEMWE.

The use of a solid membrane allows for a compact build with a minimum amount of liquid in the PEMWE cell. Nevertheless, the costs of a PEMWE stack still amount to a significant proportion of the overall system, with indicative reports quoting 37 % of the total costs of a PEMWE system [21]. Innovation in stack design and manufacture is pushing cost down and improving durability and efficiency. For example, Chisholm et al. [22] 3D printed and silver-coated PEMWE flow plates from polypropylene. These flow plates were about 4 times lighter and 5 times cheaper than conventional plates from titanium and showed good stability over 100 hours at 0.25 A cm^{-2}. Another approach to use additive manufacturing for PEMWE parts was taken by Yang et al. [23], who used selective laser melting to create a multifunctional plate incorporating LGDL, gasket, flow-plate and end-plate. By removing the contact resistance between these parts, an increase in hydrogen generation of more than 60 % was achieved.

3 Sources of Loss in a PEMWE

The decomposition of water is driven by heat and electrical energy. The minimum electrical energy required for the decomposition of water is the reversible voltage $\mathrm{V}_{rev} = 1.23\,V$, while the thermoneutral voltage $\mathrm{V}_{tn} = 1.48\,V$ is required if no external heat is supplied [24].

V_{rev} is the minimum, thermodynamic potential necessary to drive the water-splitting reaction at standard conditions. However, several other voltage contributions have to be accounted for, which constitute the operational voltage V [25–27].

$$\mathrm{V} = \mathrm{V}_{oc} + \mathrm{V}_{act} + \mathrm{V}_{ohm} + \mathrm{V}_{con} \tag{1}$$

Here, V_{oc} is the open circuit voltage, which depends on the reversible voltage V_{rev} [25]:

$$\mathrm{V}_{oc} = \mathrm{V}_{\mathrm{rev}} + \frac{RT}{2F} \ln\left(\frac{p_{H2}\sqrt{p_{O2}}}{a_{H2O}}\right) . \tag{2}$$

T denotes the temperature, R is the universal gas constant, F is the Faraday constant, and p is the partial pressure of a gas. The activity a of liquid water is 1. The open circuit voltage is the energy thermodynamically required to drive the water-splitting reaction and can be derived from the Nernst

equation [25]. It can be understood as the representation of the thermodynamic processes at the electrode.

V_{act} is the activation overpotential, which is associated with the activation energy of the water electrolysis reactions and can be described by the Butler-Volmer equation. The equation given here is most commonly used in the literature [11,25,27–31] and does not account for the liquid water saturation at the electrode surface. However, there are several examples given of the Butler-Volmer equation, incorporating the electrode surface or similar parameters [26,32,33].

$$\mathrm{V}_{act} = \mathrm{V}_{act,an} + V_{act,cat} = \frac{RT}{\alpha_{an}F}\sinh^{-1}\left(\frac{i}{2i_{0,an}}\right) + \frac{RT}{\alpha_{cat}F}\sinh^{-1}\left(\frac{i}{2i_{0,cat}}\right) \quad (3)$$

Anode and cathode contributions are denoted by an and cat, respectively. Typical values for the charge transfer coefficients are $\alpha_{an} = 2$ and $\alpha_{cat} = 0.5$ [11]. The exchange current density is denoted by i_0. The current density i is the current I normalized by the geometric active area A of the PEMWE. The exchange current density is calculated from the activation energy E_A at the respective electrode and a reference value $i_{0,ref}$ which is obtained from literature or fitting experimental polarisation data [32]:

$$i_0 = i_{0,ref}\,exp\left(-\frac{E_A}{R}\left(\frac{1}{T} - \frac{1}{T_{ref}}\right)\right)$$

The activation overpotential represents the kinetic characteristics of the electrode processes, and as such can be significantly influenced by electrode and catalyst microstructure and morphology. A more detailed discussion of electrode kinetics and the use of the Butler-Volmer equation for water electrolysis can be found elsewhere [34].

The ohmic overpotential V_{ohm} is caused by the ohmic resistance R of the different parts of the PEMWE, which consists of end-plates, ep, flow-plates, fp, liquid-gas diffusion layers, $lgdl$ and the catalyst coated membrane, ccm [25,26,35]:

$$V_{ohm} = RI = \left(R_{ep} + R_{fp} + R_{lgdl} + R_{ccm}\right)I \ . \quad (4)$$

The ohmic overpotential reflects the flow of current through a number of components from the external current connectors to the electrode surface. The conduction of current through these components requires a certain level of energy, which is expressed as an ohmic loss. The ohmic resistances above contain a portion which is attributed to the contact resistance between the respective part and the adjacent PEMWE component. This contact resistance can contribute significantly to the overall PEMWE voltage [23].

The concentration overpotential V_{con} is caused by limitations in the supply of reactant or the blockage of active catalyst sites by an excess of product. This occurs in particular at high current densities when high flow rates of water are required, and large amounts of oxygen and hydrogen are produced. From the inlet, water is transported through the flow channels and has to cross the porous LGDL to reach the active catalyst sites on the surface of the membrane. Simultaneously, the product gas is produced at the CCM and needs to move through the LGDL in counter-current flow to the water. As the mass flow through the LGDL is increasingly inhibited by the increasing amount of water and gas, additional energy is required to overcome this resistance. To provide this excess energy, an increased voltage has to be supplied to the PEMWE, which is the concentration overpotential.

The concentration overpotential is modelled as a logarithmic increase for product (O_2, H_2) concentrations at the membrane me exceeding the concentrations at a reference state 0. This definition was introduced for PEMWEs by Marangio et al. [27] and has been followed by the vast majority of publications [25,26,28,30,35–37].

$$V_{con} = V_{con,an} + V_{con,cat} = \frac{RT}{4F}\ln\left(\frac{c_{O2,me}}{c_{O2,me,0}}\right) + \frac{RT}{2F}\ln\left(\frac{c_{H2,me}}{c_{H2,me,0}}\right) \quad (5)$$

The concentration c of the species at the membrane me depends on the gas generation rate, but also at the rate of mass transport through the LGDL and flow channels.

The polarisation curve of a PEMWE, which is the sum of the contributions described above, is shown in Figure 2 (a) for different temperatures, while a theoretical *i-V* curve with a rapid voltage runaway due to the concentration overpotential is displayed in Figure 2 (b).

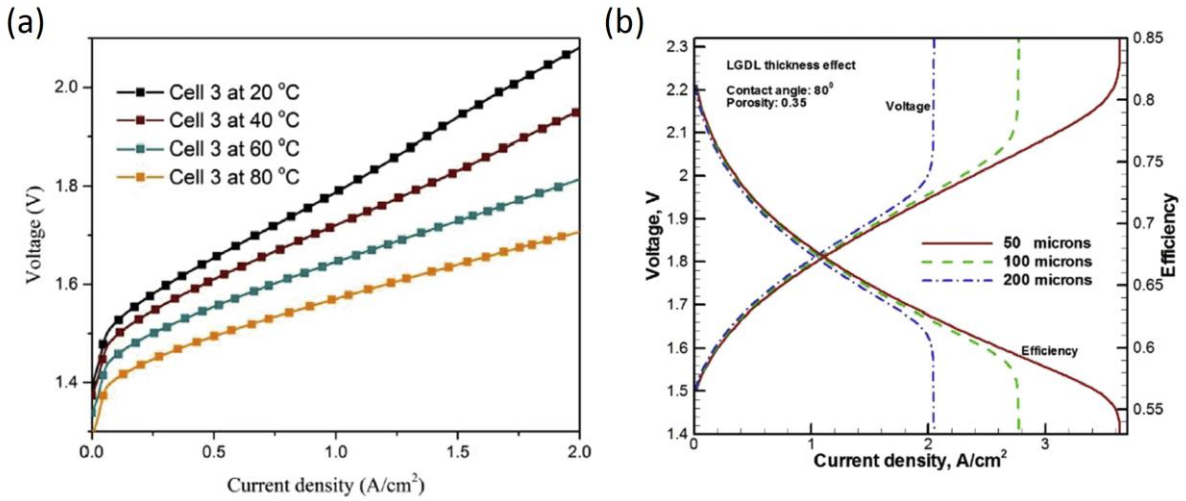

Fig. 2: (a) Polarisation curve of a PEMWE at different temperatures [38] (Reprinted from 'J Power Sources, 396, Yang et al., Bipolar plate development with additive manufacturing and protective coating for durable and high-efficiency hydrogen production, 590–8, 2018', with permission from Elsevier). **(b)** Theoretical polarisation curve, predicting rapid voltage increase due to the concentration overvoltage [26] (Reprinted from 'Int J Hydrogen Energy, 42, Han et al., Modeling of two-phase transport in proton exchange membrane electrolyzer cells for hydrogen energy, 4478–89, 2017', with permission from Elsevier).

4 Mass Transport in the Flow Channels

4.1 Flow Regime

Flow-fields ensure the supply of the electrolyser with water and the removal of product gas. While water supply is only necessary on the anode side, flow-fields are also often used on the cathode side to facilitate removal of hydrogen and excess water. The following discussion focuses on the processes on the anode side; however, many aspects apply to the cathode as well.

Depending on the amount of oxygen produced, the flow regime can vary from single-phase flow (no oxygen production) to several different forms of two-phase flow. As current density is increased a range of flow regimes can be observed, with varying descriptions used in the literature. It is not uncommon to find identical flow regimes being described by different terms or identical terms

describing slightly different flow regimes. In this review, the classification of flow regimes according to Mishima et al. [39] is used throughout.

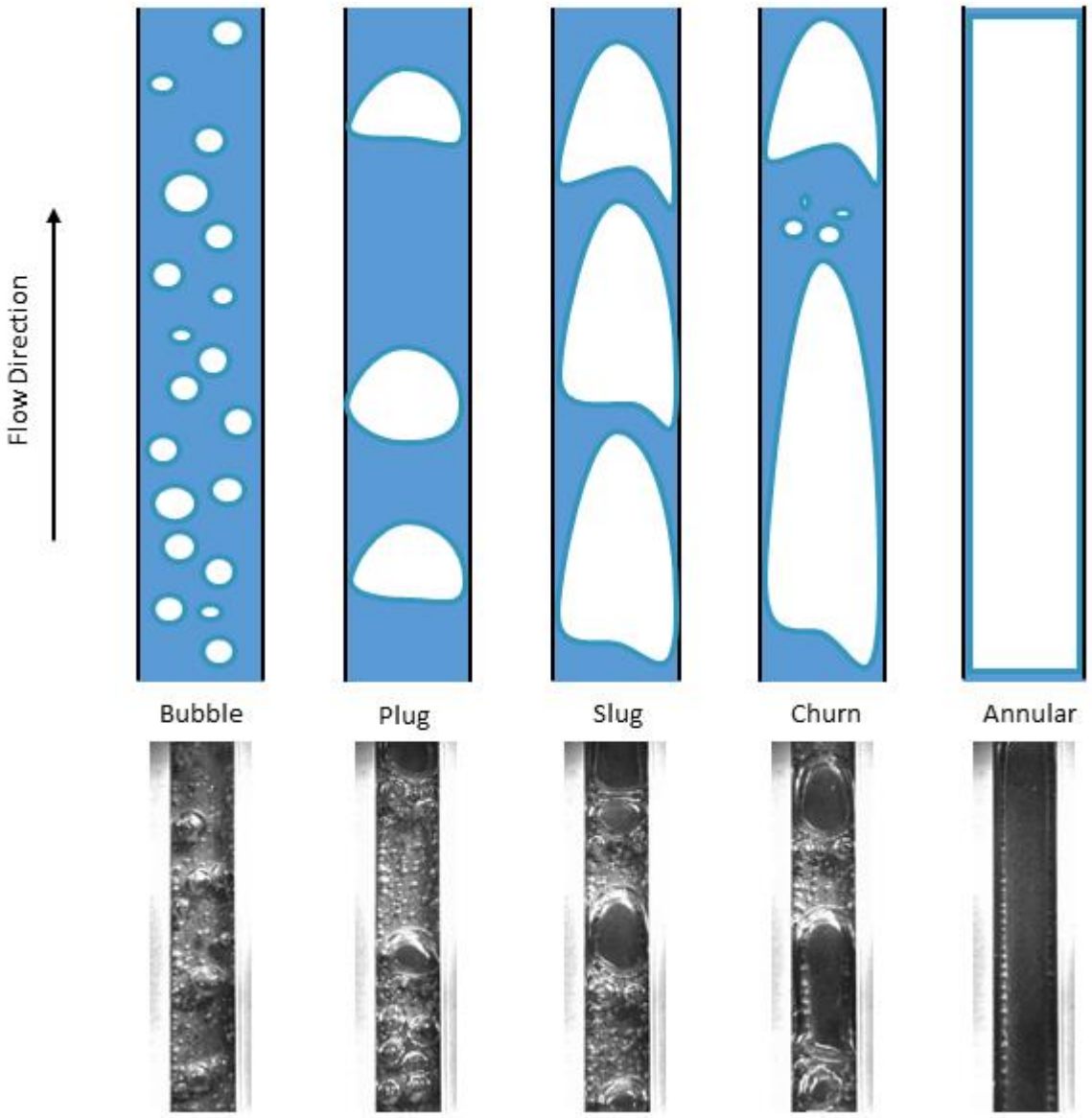

Fig.3: With increasing current density, more gas is produced and has to be removed through the flow channels. The flow regime progresses from bubble to plug, slug, churn and annular regime.

Figure 3 describes the development of flow regimes with increasing gas-to-water ratio. With the onset of electrochemical activity and related gas production the flow regime changes from single-phase water flow to bubbly flow. As more gas is produced, bubbles coalesce to form plugs then slugs, filling the entire diameter of the tube or channel. In churn flow, slug bubbles are deformed and no longer

display a spherical shape. The liquid between gas slugs is increasingly filled with small gas bubbles. As flow transitions into annular, the remaining water forms a film along the channel wall, while the rest of the channel is almost exclusively filled with gas. A further increased gas flow disperses the liquid film along the wall. Hence, the whole channel is filled with a gas-liquid dispersion; this is classified as annular-mist flow [39].

4.2 Mass Flux

To link the electrochemical activity of a PEMWE to the flow regime in its flow channels, a flow map can be developed. This requires knowledge of the rate of water consumption and oxygen gas generation; the necessary equations are presented in the following normalised to the cross-sectional area of individual flow channels. Water is consumed by the oxygen evolution reaction (OER) on the anode side at a given rate by [40]:

$$G_{cons} = \frac{iAM_{H2O}}{2Fn_{chan}a} \,. \tag{6}$$

Here, i is the current density, A is the active area of the electrolyser, M_{H2O} is the molecular mass of water, F is the Faraday constant, n_{chan} is the number of flow channels and a is the cross-sectional area of a flow channel.

At the same time, water is removed from the anode side of the PEMWE due to electro-osmotic drag. This is caused by protons moving from anode to cathode through the polymer membrane. The rate of water removal by this process is defined by [40]:

$$G_{drag} = n_{drag}\frac{iAM_{H2O}}{Fn_{chan}a} \,. \tag{7}$$

The number of water molecules transported through the membrane per proton is defined by the temperature-dependent electro-osmotic drag coefficient n_{drag}. Commonly, an empirical approximation by Onda et al. is used in PEMWE literature [41]:

$$n_{drag} = 0.0134\,T + 0.03 \,. \tag{8}$$

The rate of oxygen production is calculated as [40]:

$$G_{O2} = \frac{iAM_{O2}}{4Fn_{chan}a}\,, \tag{9}$$

where M_{O2} is the molecular mass of oxygen.

As water molecules are dragged from the anode to the cathode, oxygen and hydrogen dissolved in the water are also transported across the membrane to the cathode. While the dragged hydrogen reduces the net gas crossover as it is the opposite direction of hydrogen permeation, the drag of dissolved oxygen adds to the oxygen permeation and causes further side reactions at the cathode and a reduction in PEMWE efficiency [24,42].

The gravimetric gas fraction x can be calculated from the above mass fluxes and the total rate of water circulation into the anode side of the PEMWE. It is the ratio of gas generation rate (G_{O2}) to the total mass flux in the channel, which is the sum of the water mass flux ($G_{circ} - G_{cons} - G_{drag}$) and gas generation rate [40].

$$x = \frac{G_{O2}}{G_{circ} - G_{cons} - G_{drag} + G_{O2}} \tag{10}$$

It should be noted that x is dependent on the location along the flow channel. To calculate x for a position before the outlet, the active area A has to be reduced accordingly.

Another metric to characterise the flow in the PEMWE is the water ratio ζ, which is defined as the ratio of the rate of water circulation to the rate of water removal by the combination of the OER and electro-osmotic drag [40,43].

$$\zeta = \frac{G_{circ}}{G_{cons} + G_{drag}} \tag{11}$$

Theoretically, a value of ζ=1 is sufficient for electrolysis. However, in practice, a higher value is required to ensure sufficient water supply and cooling. Minimum, safe values for the water ratio found in the literature range from ζ=3 [43] to ζ=5 [40]. A comparison of water flux and gas generation, and the gas fraction at the outlet, as a function of current density is shown in Figure 4 (a) and for the water ratio in Figure 4 (b).

The flow velocity of liquid j_l and gas j_g can be calculated as a function of the gas fraction [40].

$$j_l = \frac{G(1-x)}{\rho_{H2O}} = \frac{(G_l + G_g)(1-x)}{\rho_{H2O}} = \frac{(G_{circ} - G_{cons} - G_{drag} + G_{O2})(1-x)}{\rho_{H2O}} \tag{12}$$

$$j_g = \frac{Gx}{\rho_{O2}} \tag{13}$$

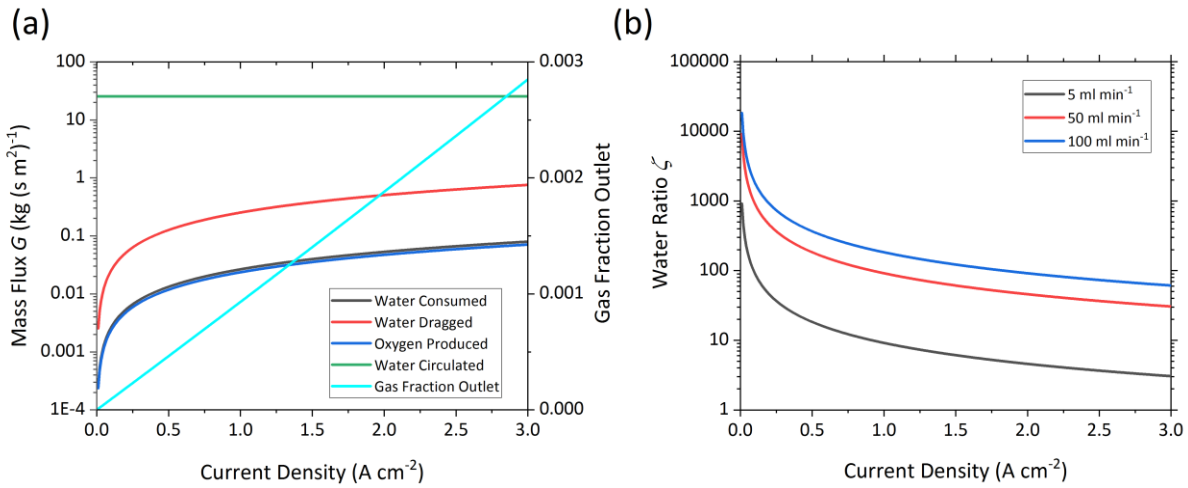

Fig.4: (a) Comparison of the mass fluxes of water with the oxygen generation in the range from 0.0 A cm^{-2} to 3.0 A cm^{-2} at a water circulation rate of 50 ml min^{-1}, a temperature of 90 °C, in a parallel flow-field with 9 channels (Width: 1.76 mm, Depth: 2 mm). The gravimetric gas fraction at the outlet increases linearly with current density. **(b)** Water ratio as a function of current density at the same conditions, for water circulation rates of 5 ml min^{-1}, 50 ml min^{-1}, and 100 ml min^{-1}.

Here, the total flow through the flow channels G consists of the total liquid flow G_l and gas flow G_g. The flow velocities of gas and liquid can be used to compare the state of operation of a PEMWE with known flow maps to define the flow regime in the flow channels. For comparison, attention has to be paid to choose a flow map which was observed in a system as similar as possible (materials and geometry) to the flow channels of the PEMWE. Two flow maps commonly used for research relating to PEMWEs are shown in Figure 5.

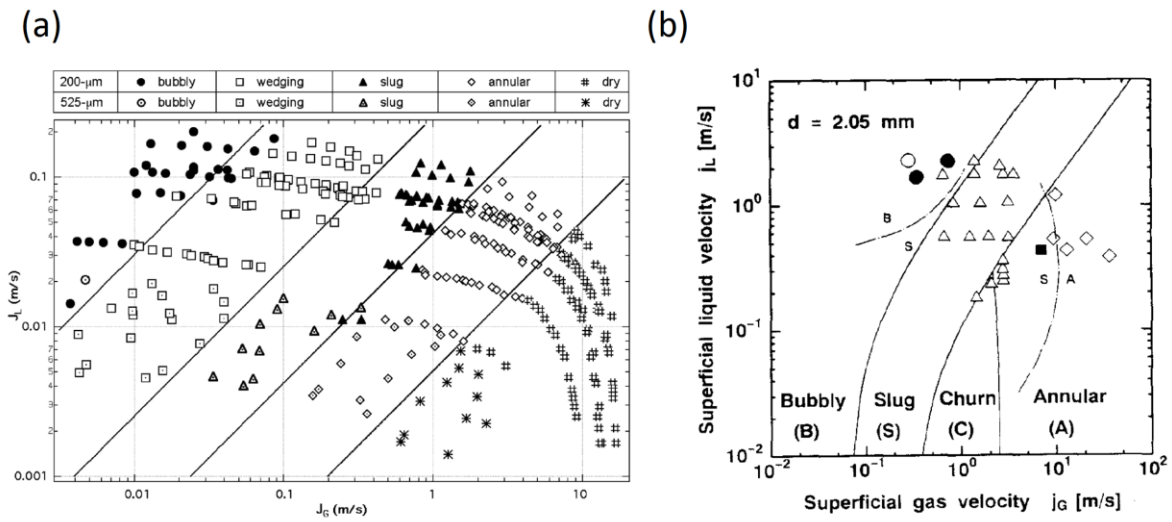

Fig.5: The flow maps of **(a)** Cubaud et al. [44] (Reprinted from 'Cubaud et al., Transport of bubbles in square microchannels. Phys Fluids 2004;16:4575–85.', with the permission of AIP Publishing.) and **(b)** Mishima et al. [39] (Reprinted from 'Int J Multiph Flow, 22, Mishima et al., Some characteristics of air-water two-phase flow in small diameter vertical tubes, 703–12', with permission from Elsevier), defining the occurrence of various flow regimes as a function of the velocity of the liquid and gas phase in the flow channels. The shape and location of the regime borders vary depending on the exact shape and size of the channels of the experimental systems used to create the flow map.

4.3 Flow-Field Design and Diagnostics

The design of the flow-field affects pressure drop, gas and water flow velocities, gas removal, and the flow regime. Most commonly described in the literature are parallel, single-serpentine, and multiple-serpentine flow-fields. Each design varies in the amount of water and gas that is transported through an individual channel (Figure 6). Other flow-field geometries, such as interdigitated [45–47] or pin-type [23,48] flow-fields, exist but are not very commonly used.

The flow-fields introduced here are typically used for PEMWE research and the most commonly discussed geometries in scientific literature. However, other alternatives are possible, such as the use of metal meshes as flow-fields, which are used in proprietary commercial PEMWE systems.

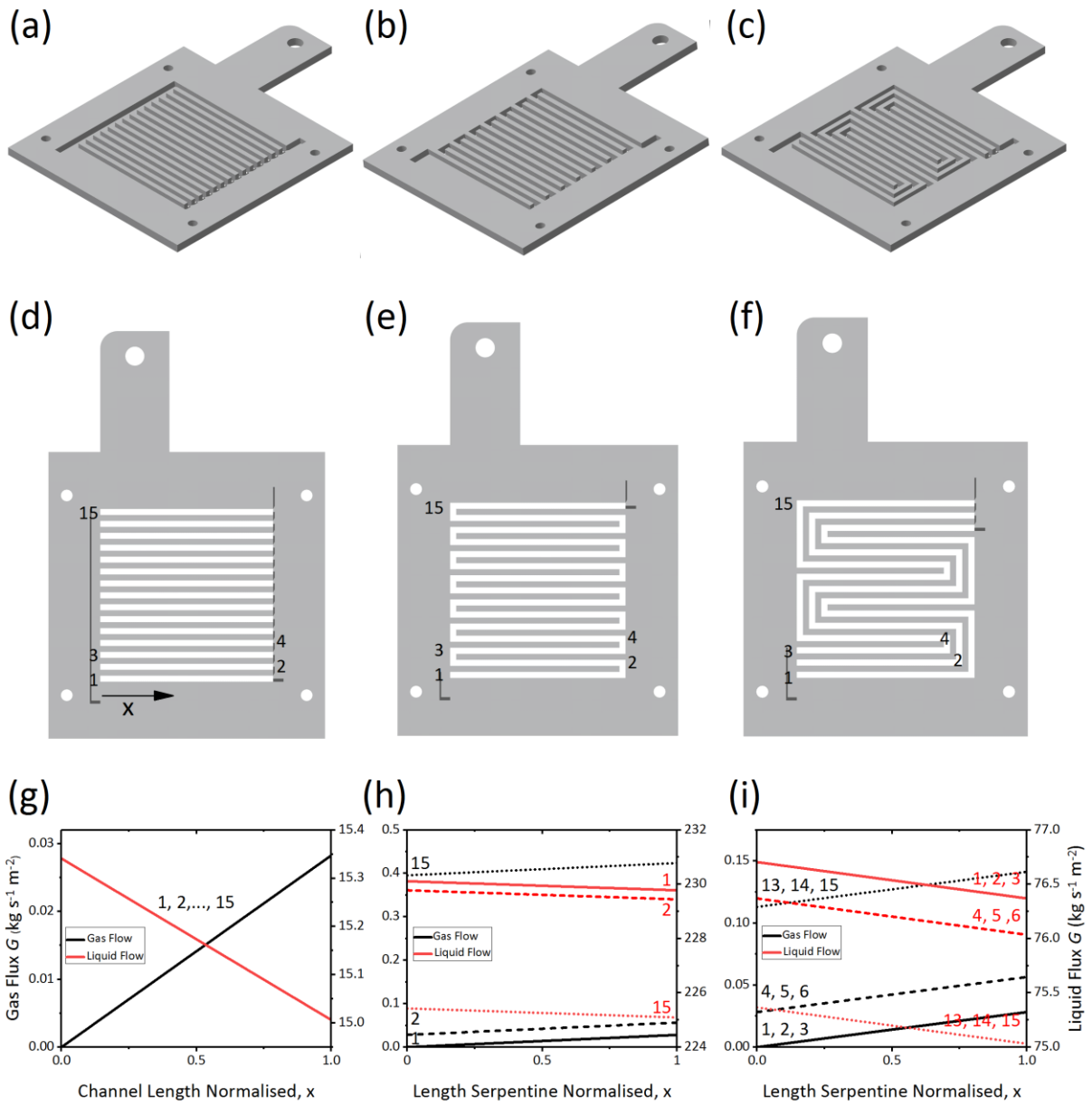

Fig. 6: Perspective **(a-c)** and top-down **(d-f)** view of a parallel **(a,d,g)**, single-serpentine **(b,e,h)**, and triple-serpentine **(c,f,i)** flow-field. The gas and liquid amount in each channel along its length **(g-i)** varies depending on the flow-field geometry. The channel number is indicated in **(d-f)** and used accordingly in **(g-i)**. The axis titles on the left and right of **(g-i)** apply to all three figures.

In parallel flow-fields (Figure 6 (a),(d),(g)), the flow is separated into a number of separate channels, which are connected by a dividing and a combining manifold. Usually, parallel flow-plates are designed in a Z-pattern, with inlet and outlet located at diagonally opposing corners of the flow-field. Ideally, the amount of water and gas passing through an individual channel is the corresponding fraction of

the total amount of water and gas with respect to the total number of channels. However, if a flow-field with a Z-pattern is used, a non-uniform distribution of flow occurs [49]. For a single-serpentine flow-field (Figure 6 (b),(e),(h)), all of the water and gas has to pass through one channel, thus causing much higher flow velocities than in a parallel flow-field. Hence, the pressure drop in a single-serpentine flow-field is significantly higher than for a parallel flow-field [40].

There is conflicting information on the performance of these flow-fields. Ito et al. [40] showed improved performance of a PEMWE (active area: 5.2 x 5.2 cm) with a parallel flow-field up to 1.0 A cm^{-2}. They assigned this difference in performance to an increased concentration overpotential in the single-serpentine flow-field. However, it is unlikely that this effect is notable at current densities as low as 1.0 A cm^{-2}. Majasan et al. [50] also found improved performance for the parallel flow-field for current densities of up to 3.0 A cm^{-2}, whereas, Li et al. [51] showed superior performance of a single-serpentine flow-field. In this study, the parallel flow-field was also shown to have the highest ohmic resistance, which partly explains the decreased performance. This raises the question if the dominant factors influencing electrochemical performance of different flow-fields are flow effects or simply the ohmic resistance of the flow-plate. In the latter case, further work is necessary to optimise flow-field geometry by minimising ohmic resistance (channel-to-land ratio) while ensuring a sufficiently low pressure drop. Also, further work on the exact role of flow effects on electrochemical performance is required.

Multiple-serpentine flow-fields (Figure 6 (c),(f),(i)) share characteristics of the parallel as well as the single-serpentine flow-field. Their electrochemical performance and pressure drop were found to be intermediate to those of parallel and single-serpentine flow-fields [40].

All flow-fields shown in Figure 6 are of the Z-type, with inlet and outlet being located at diagonally opposed sides of the active area (bottom left and top right). Alternatively, flow-fields can be designed in a U-shape, which would require inlet and outlet being located at the same side of the active area

(e.g. bottom left and top left). The location of inlet and outlet has been shown to have significant impact on the distribution of water flow between individual channels of a flow-field [49,52,53].

There is very little published research examining possibilities to optimise flow-fields beyond the differentiation of parallel, single and multiple-serpentine designs. Majasan et al. showed that the performance of a PEMWE is affected by the depth of the flow channels and demonstrated a varying degree of mass transport limitation with flow channel depth at different current densities. A non-monotonic trend was found, implying the possibility of optimising the flow-field design [54].

A multitude of approaches have been deployed to image and diagnose the processes in the flow channels of PEMWEs. Most publications use either optical, X-ray or neutron imaging to visualize bubble and water flow. Optical imaging is comparatively low-cost and easy to implement, which makes it a preferred tool for flow-field diagnosis [55–62]. X-ray and neutron imaging, on the other hand, are expensive, require large-scale facilities, and often the PEMWE cell needs to be adapted or miniaturized to facilitate measurement. However, these techniques offer quantitative capabilities and the possibility of analysing the processes in the flow-field, LGDL and catalyst layer simultaneously, which explains the attraction of X-ray [63,64] and neutron imaging [65–69] techniques for the study of PEMWEs. X-ray imaging usually offers a higher flux and therefore shorter acquisition times, while the preferential attenuation of neutrons in hydrogen and water makes neutron imaging an especially valuable diagnostic tool [70].

While imaging techniques offer valuable insight into flow processes, they suffer obvious drawbacks in terms of cost and ease of implementation and are often not suited as diagnostic tools for industrial PEMWE plants. To mitigate these disadvantages Maier et al. [71] used acoustic emission (AE) as a non-destructive, *operando* diagnostic tool to diagnose the relative change of bubble size and number of bubbles in the flow channels of a PEMWE. This allowed for the identification of the transition from bubbly to slug flow.

4.4 Influence of the Flow Regime on Performance

There are essentially two model concepts on how the flow regime can affect the overall performance of a PEMWE. The first idea assumes that the formation of gas slugs in the flow channel hinders the supply of water to the LGDL, and consequentially to the catalyst sites. This would then decrease overall performance by amplifying the concentration overpotential [72]. The second concept assumes that the bubbles in the flow channel cause turbulence which leads other bubbles in the vicinity to detach from the LGDL surface. This effect gets stronger when the size of bubbles in the flow channel increases. Hence, bubbles are effectively removed from the LGDL surface, which accelerates gas removal from the catalyst sites and through the LGDL. This would cause a decrease in concentration overpotential [56].

Ito et al. [40] measured the performance of a PEMWE, comparing three different flow-field designs: parallel, single-serpentine, and dual-serpentine. As shown in Section 0, the water flow speed, water-to-gas ratio, and flow regime vary widely between these designs even at identical operating conditions. In particular, flow-fields with fewer flow channels (serpentine) favour the development of flow regimes with a low water-to-gas ratio (slug, annular), while flow-fields with multiple channels (parallel) favour flow regimes with a higher water-to-gas ratio, such as bubbly flow. As the authors observed a decrease in performance from the parallel to single-serpentine and then dual-serpentine flow-field, they concluded that performance deteriorates for flow regimes with a lower water-to-gas ratio than bubbly flow [40].

In later work, Ito et al. [72] examined the occurrence and pressure drop of different flow regimes and the link between the mean pore diameter of the LGDL and the development of the flow regime. Their theoretical considerations and experimental data imply that a LGDL with bigger pores results in a larger bubble detachment diameter and hence plug and slug flow are reached at lower current densities compared to a LGDL with smaller pores. This leads to vast areas of the liquid-gas diffusion layer being covered by gas bubbles, which they postulated had a negative effect on performance. In

subsequent work, the authors [73] measured the cell resistance and overall performance using titanium felts of different pore size as LGDLs. An increase in cell resistance with increasing pore size was found, which is attributed to an increase in bubble detachment radius.

Sun et al. [43] performed current mapping and localised electrochemical impedance spectroscopy (EIS) on a PEMWE under water starvation; they showed that in the case of water starvation, performance decreases under slug and churn flow compared to the bubble regime. Similar observations of the decrease of local current density towards the end of the channel under water starvation have been made by Immerz et al. [74,75]. However, both authors compared subsequent locations along the flow in a PEM water electrolyser and not a whole cell under different regimes. Therefore, it is uncertain if these results can show the influence of the flow regime properly, as flow regime and water starvation effects occur at the same time.

Using EIS and high-speed imaging, Dedigama et al. [55] came to a contrary conclusion; their results showed an improvement in mass transport, which is associated with the transition from bubble to slug flow. Further, Dedigama et al. [56] mapped the current density at different locations along a single-channel PEMWE and found an increase in performance towards the top end of the channel and showed that slug flow is the dominant flow regime at this location. This supported the earlier finding that performance is enhanced in slug flow. However, it has been proposed that this might be caused by an increase in temperature along the flow channel [76]. Further, the increase in mass transfer inhibition at higher flow rates can be seen as a consequence of the increased kinetic energy of water flow in the flow channel, which hinders the detachment of gas bubbles from the LGDL surface into the flow channel [77].

There is a lack of consensus and understanding of the exact relationship between PEMWE performance and the flow regime. Further, to date, no coherent model of the processes underlying potential performance changes due to a specific flow regime has been developed and backed by conclusive experimental data.

4.5 Two-Phase Modelling

Modelling of the two-phase flow offers the opportunity to predict the effects of changes to geometry or physical parameters in a low-cost and rapid way. For every modelling work the underlying assumptions have to be studied carefully to understand the possibilities and limitations of a given model. Details on the used assumptions can be found in individual publications, but common examples include an even distribution of current and temperature across the active area [46], limitation to single-phase flow [78], or restricted validity to one specific domain, e.g. the anode flow channels [49].

Only a few publications have provided comprehensive 3D models incorporating two-phase flow, specifically aiming at PEMWEs [45–47]. Lafmejani et al. [47] published a 3D volume-of-fluid model and qualitatively confirmed their results with optical imaging of the flow in an interdigitated flow-field. Olesen et al. [45,46] presented a full-scale, mathematical, 3D model of a PEMWE, incorporating compressible two-phase flow as well as heat and charge transfer in the catalyst layer, micro-porous layer, LGDL and the flow channels. The authors used this model to predict the state of operation of a PEMWE for current densities up to 5.0 A cm^{-2}. For these elevated currents they found a heterogeneity in the current density distribution of up to 1.5 A cm^{-2} and in the temperature distribution of up to 20 K. Further, they showed that changing the design of an interdigitated flow-field design can lead to significant variations in local temperature, which can accelerate catalyst degradation, while the overall cell performance with these flow-fields did not differ. This work also highlights the particular value of two-phase modelling for high current density operation, as the link between uneven water-gas distribution and hotspot formation is demonstrated [45]. This shows the significant effect mass transport aspects can have at elevated current density and how two-phase modelling can be used to investigate these effects.

The work described above mathematically incorporated the two-phase flow in the LGDL without explicitly describing the movement of gas and water. Resolving the exact transport pathways of gas

bubbles through the LGDL enables to study the effect of LGDL microstructure on mass transport, but it is challenging to link this to the overall PEMWE performance [79].

Other approaches to PEMWE flow modelling are limited to one-phase flow [31,49,80]. Nie et al. [49] simulated one-phase flow through a parallel flow-field with a Z-pattern. In this type of flow-field, the water inlet is positioned diagonally opposite the water outlet and it is commonly used in PEMWEs. The authors showed that for this type of flow-field the water flow velocity is very unevenly distributed between the single flow channels. The Z shape favours flow through the flow channels closest to the outlet which causes the water flow velocity to be up to five times higher than in the middle channels. Further, the authors found a corresponding pressure maldistribution over the flow-field, with the pressure roughly decreasing diagonally from inlet to outlet.

Toghyani et al. used single-phase flow modelling to address the optimization of standard flow-fields and development of novel flow-field designs. The authors showed that serpentine flow-fields with a varying number of flow channels caused an improved electrochemical performance and lower temperatures compared with a parallel flow-field [31]. They also explored the use of metal foam as a flow-field material and concluded that the electrochemical performance of a PEMWE could be improved by this [81], and modelled the flow through a novel, spiral flow-field geometry [82].

5 Mass Transport in the Liquid-Gas Diffusion Layer

Fluid flow through a porous medium, such as the LGDL, is a highly complex process which is affected by the microstructure of the porous medium, interfacial interactions between fluid and walls, interactions between different fluids, and bulk properties of the fluids. This makes it challenging to analytically describe multi-fluid flow in porous media and numerous equations have been developed, each describing specific situations and introducing additional parameters to achieve improved precision. However, the most fundamental (and most modified) equation for fluid flow in porous media is Darcy's law, which links the fluid velocity u to its pressure gradient across a control volume

$\frac{\partial p}{\partial x}$ [83]. It is commonly used in computational work on PEMWEs [26,47,84,85]; however, variations of Darcy's law are sometimes employed to achieve higher accuracy [46,78].

$$u = -\frac{K}{\eta}\frac{\partial p}{\partial x} \tag{14}$$

Darcy's law takes into account the permeability of the fluid K and its viscosity η. The permeability can be calculated from various equations, as well as empirical correlations [46,47], but the Kozeny-Carman equation is the best-known approach. It links the macroscopic permeability with the microscopic parameters of the porous medium porosity ε, tortuosity τ, and the surface area per unit volume a_V, but various modifications and extensions have been discussed [83].

$$\sqrt{\frac{K}{\varepsilon}} = \left(a_V\sqrt{2\tau}\right)^{-1}\left(\frac{\varepsilon}{1-\varepsilon}\right) \tag{15}$$

5.1 LGDL Materials

The liquid-gas diffusion layer serves a multitude of purposes; it is expected to provide good thermal and electrical conductivity, low interfacial losses and mechanical strength and support for the flexible CCM, especially under differential pressure operation. Furthermore, the LGDL needs to withstand the corrosive environment on the anode side during long-term operation without degradation or forming a passivating layer. This requirement makes titanium the most commonly used material for the LGDL on the anode side. However, recent work by Becker at al. [86] has shown that, away from the catalyst layer/LGDL interface, the corrosion potential at the surface of the anode LGDL is decoupled from that of the catalyst layer due to the low conductivity of the water phase. This opens up the possibility of use of cheaper LGDL materials such as carbon and carbon-coated stainless steel, which are also easier to manufacture into porous structures than titanium.

Another crucial purpose of the liquid-gas diffusion layer is to facilitate the two-phase counter-current flux of gas towards the flow channels and water towards the CCM. Hence, the microstructure of the LGDL needs to be optimized with respect to the trade-off between mass and electron transport, with

mechanical stability, thermal conductivity and good interfacial contact as further constraints [11,57,87]. Especially the interface between LGDL and catalyst layer appears to have a strong influence on contact resistance, charge and mass transfer resistance [88–90]. Due to the multiple functions of the LGDL the choice of material has a significant impact on the operation, performance, and mass transport characteristics of a PEMWE. Choosing an adequate LGDL material for a PEMWE application is essential to guarantee stable and good performance.

Porous titanium sintered or fibrous materials have been most commonly used as LGDLs. In some cases, titanium meshes have been used as the LGDL, while recently the use of thin, perforated plates has been proposed as a beneficial alternative to more established materials. Another potential material that has been adopted as LGDL in PEM fuel cells (PEMFCs) are metal foams. SEM images and X-ray tomograms of these materials are shown in Figure 7, visualizing the surface and microstructure of the LGDL materials.

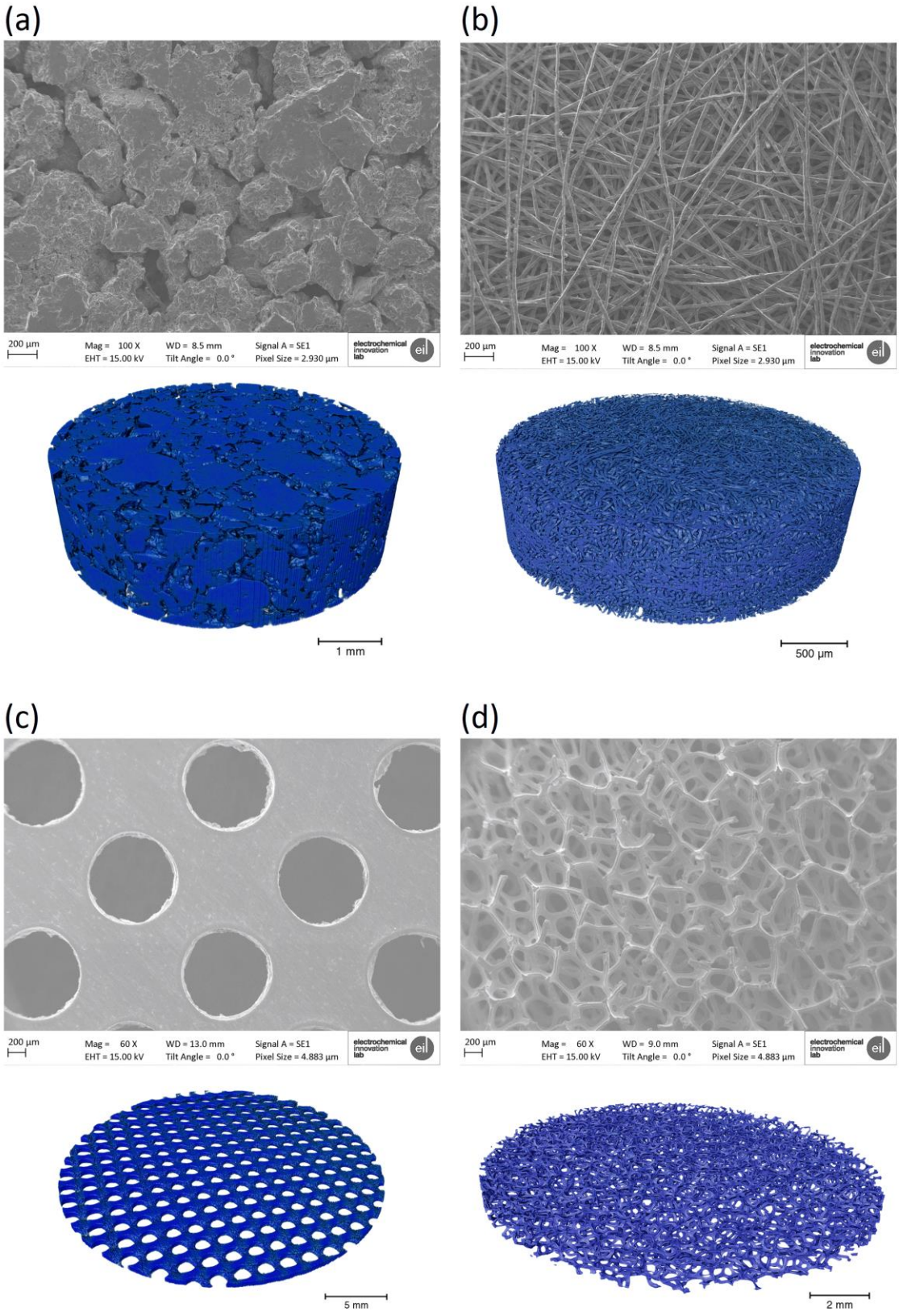

Fig.7: SEM images and X-ray Tomograms of various materials that can be used as a LGDL in PEMWEs. **(a)** Sintered powder and **(b)** fibrous materials are commonly employed, while **(c)** perforated plates are very useful for optical access to the catalyst surface, and **(d)** metal foams have shown promise in unitized reversible fuel cells.

Porous titanium sinters (Figure 7 (a)) have been widely used as a LGDL, e.g. in the PEMWE stacks developed for the GenHyPEM project [91–94]. Grigoriev et al. [95] have published a study that theoretically and experimentally examines the influence of different sinter properties on PEMWE performance. They concluded that 50 µm to 75 µm is the optimal titanium powder particle size, resulting in a LGDL pore mean diameter of 12 µm to 13 µm after sintering, which has recently been confirmed [96]. Other conclusions are that pore size and electrical resistance have a big influence on the performance of the LGDL, while porosity and gas permeability appear to be insignificant. However, this applies only when the porosity lies between 30 % and 50 %, which has been identified as the optimal range based on theoretical considerations.

In recent years, titanium fibrous materials (Figure 7 (b)) have emerged as a potential alternative to sintered LGDL materials. These felts have very high porosities of more than 70 %, which is significantly higher than for a typical sinter. Ito et al. have tested the performance of a PEMWE using various felts, varying pore sizes and porosities. They showed that performance increases with decreasing pore sizes above 10 µm, which is assigned to the mass transfer inhibitions related to larger gas bubbles. Furthermore, the results indicate that within the range of examined materials the porosity does not seem to affect the performance [72,73].

Another recent development is the use of perforated plates or foils (Figure 7 (c)) as LGDLs. The manufacturing of perforated titanium foils by mask-patterned wet etching methods and their potential application as LGDL was first described by Mo et al. [97]. A titanium foil is covered with photoresist and the pattern of pores is then developed using a photomask manufactured by soft lithography. Subsequently, the pores are etched into the foil with hydrofluoric acid. After removing the remaining photoresist, a pristine LGDL with regular, straight pores and easily tuneable features is obtained [87]. These thin, novel LGDLs have been shown to exhibit significantly superior performance compared to titanium felt, which is caused by the increased interfacial contact between LGDL, flow-field, and CCM [98]. In a later study, Kang et al. [99] manufactured gold coated, perforated titanium

foils and demonstrated a reduced operating voltage at high current densities and stability of the gold coating for 100 hours was shown.

A rarely applied alternative for LGDLs are titanium meshes. Li et al. [100] showed that the pore size of the mesh is crucial for performance at high temperatures, but less so at low temperatures. Steen et al. [101] tested various meshes, but even the mesh with optimum parameters performed significantly worse than titanium felt. Titanium meshes can also be used as low-cost flow-field, an alternative especially used for proprietary commercial systems.

For the future development of LGDLs in PEMWEs, metal foams (Figure 7 (d)) appear to be very promising. Baumann et al. [102] sprayed catalyst ink directly onto titanium foam and used this as combined LGDL and electrode in a PEMWE. This demonstrated the feasibility of deploying metal foams in PEMWEs; however, a systematic study evaluating the role of metal foam as LGDL was not carried out. Titanium foam has also been used as the LGDL in a unitized reversible fuel cell (URFC), which can operate in either fuel cell or electrolysis mode, and good performance in electrolysis mode was demonstrated [103]. Arisetty et al. [104] used nickel foam as combined LGDL and flow-field in a direct methanol fuel cell and showed that this configuration can outperform a classical flow-field/LGDL combination. The idea of combining LGDL and flow-field by using nickel foam was later also applied in PEMFCs and was shown to yield superior performance compared to the use of separate LGDL and flow-field [105]. To this point, only a computational study on the use of metal foam as flow-field in a PEMWE exists (see Section 4.5) [81]. Further research on the use as a LGDL is necessary.

5.2 Micro-Porous Layers and Surface Modifications

Based on proven procedures for PEM fuel cells, modifying the surface of particles or fibres in the LGDL or introducing an additional layer to the LGDL has been widely proposed to reduce the mass transport overpotential and improve overall PEMWE performance. For PEM fuel cells, it has been shown that the introduction of a micro-porous or micro-protective layer (MPL) on the side of the gas diffusion layer neighbouring the catalyst layer benefits performance by regulating water management and gas

transport at the interface. This layer consists of carbon black or PTFE and forms a layer with smaller pores than the rest of the LGDL [106–110].

5.2.1 Micro-Porous Layer

Unfortunately, carbon or PTFE MPLs are not stable in the corrosive environment at the LGDL/catalyst layer interface at the anode of a PEMWE, therefore, other materials have been applied, trying to mimic the effect of the MPL in PEMFCs. Lettenmeier et al. [111] created a MPL by coating a titanium sinter with porous titanium via thermal spraying and demonstrated its superior performance, particularly at current densities exceeding 2.0 A cm^{-2}. Sung et al. [112] used a coating of IrO_2/Ta_2O_5 to produce a reactive MPL to convert active oxygen species to oxygen, but did not compare the performance of their system with a reference. Coating carbon paper with carbon black and subsequently with IrO_2 has been shown to yield a LGDL and MPL stable for 2000 hours, but no performance comparison to a conventional PEMWE system was made [113].

Kang et al. [59] used micro (~5 µm) and spherical nano (30 -50 nm) titanium particles to create a MPL on a LGDL with small, straight, regular pores via low-temperature air spraying. It was found that micro-particles yielded stronger performance improvement than nano-particles. A significant performance improvement (1.707 V to 1.687 V at 2.0 A cm^{-2}) was found for the micro MPL. High-speed imaging showed that the MPL increased the amount of pores providing active catalyst sites.

The effect of coatings to provide a MPL has also been investigated in unitized reversible fuel cells (URFCs). Ito et al. [114] used a layer of PTFE coating on titanium felt as the LGDL in a URFC. They found that the influence of the modified LGDL depends on fibre size, but a positive effect was only shown for fuel cell mode, not for electrolysis operation. Hwang et al. confirmed many of these findings [115] and later created a MPL on titanium felt by applying titanium powder and showed improved performance in a URFC for fuel cell operation. No performance improvement was found in electrolysis mode; however, the system was only tested up to 1.0 A cm^{-2} [116].

Building on the idea of a MPL, the use of LGDLs with graded porosity, increasing towards the flow channels, has been shown to be beneficial in PEMFCs [117–119]. Lettenmeier et al. [120] produced a sinter-like structure with a graded pore size via vacuum plasma spraying. However, the authors could not show a significant performance improvement using this novel material as the LGDL in a PEMWE. In a similar approach, Kang et al. [121] provided a gradual decrease in LGDL pore size. The authors introduced the concept of an in-plane transport enhancement layer, combining two LGDLs with straight, circular pores; one with large pores (~830 μm) neighbouring the flow channels, and a second one below it with significantly smaller pores (~100 μm). Results show a slight improvement in performance with the use of the enhancement layer. The authors attribute this to an improvement in access to pores, which before were covered by the land areas of the flow plates.

5.2.2 Surface Modification

For PEMFCs, chemical modification of the gas diffusion layer, e.g. by adding a hydrophobic agent such as PTFE, has been demonstrated to be feasible, stable, and beneficial to performance [122–125]. The chemical modification of the surface changes the contact angle of gas and water, favouring the transport of one or the other in specific areas or across the entire active area. The link between LGDL wettability (contact angle) and PEMWE performance is well established [26,100,126].

However, little work has focused on varying the wettability of LGDLs for PEMWEs. Li et al. [127] applied a hydrophobic monolayer of n-octadecyl tri-chlorosilane onto the surface of a titanium LGDL. They could not demonstrate any performance improvement compared to an untreated LGDL, but observed more frequent bubble detachment from the LGDL surface. Bystron et al. [128] etched titanium felts in hydrochloric acid, creating a titanium hydride sublayer. The authors showed significantly improved performance (voltage reduction of around 0.15 V at 0.5 A cm^{-2}) for more than 100 hours for felts treated in that manner. Kang et al. [129] measured the PEMWE performance of PTFE-treated Toray carbon paper and demonstrated a performance decrease with increasing hydrophobicity (PTFE content).

Recent work by Suermann et al. [130] demonstrated the treatment of a fibrous titanium LGDL with a femtosecond laser, inducing a high-surface structure, and showed a performance improvement linked to the reduced contact resistance.

5.3 Bubble Nucleation and Growth

Gas that is produced on the surface of the catalyst layer through electrochemical reaction forms bubbles which are then transported through the LGDL and into the flow channels. The nucleation of these bubbles is driven by the difference in chemical potential μ between gas (g) and liquid (l) phase [131].

$$\Delta\mu = \mu_l(p_g, T) - \mu_g(p_g, T) > 0 \tag{16}$$

This driving force can be expressed in terms of temperature, pressure, the Boltzmann constant k_B and the saturation pressure p_{sat} [131]:

$$\Delta\mu = k_B T \ln\frac{p_g}{p_{sat}} = k_B T \ln S \quad , \tag{17}$$

with the supersaturation S. The pressure of the gas phase p_g is linked to the overall rate of electrochemical gas production, which can be calculated using Faraday's law (see Section 4.2).

The Gibbs free energy ΔG of a cluster of n molecules is linked to the chemical potential difference, the surface tension of a planar cluster γ_∞ and the surface area of the cluster $A(n)$ [131].

$$\Delta G = -n\Delta\mu + \gamma_\infty A(n) \tag{18}$$

ΔG has a maximum for the critical cluster size n_c. Clusters with less than n_c molecules on average dissociate, while clusters with more than n_c molecules on average nucleate into bubbles [131].

$$n_c = \left[\frac{2}{3}\frac{\gamma_\infty s_l}{k_B T \ln S}\right]^3 \tag{19}$$

The liquid phase factor is expressed as $s_l = (36\pi)^{1/3} v_l^{2/3}$, with the molecular volume of the liquid phase v_l.

Increasing current density leads to a rise in gas production, which increases the supersaturation; this reduces the critical cluster size and favours the formation of new gas bubbles. However, the classical nucleation theory only describes bubble nucleation on a regular surface under specific assumptions [131]. To our knowledge, there is no published work on the nucleation of bubbles on the irregular surface of the catalyst layer under real-world conditions.

Nouri-Khorasani et al. [126] developed a model of bubble nucleation and growth and its effect on electrolysis overpotential. They identified four phases from nucleation of a bubble to its detachment from the LGDL surface. After sufficient supersaturation causes nucleation, the bubble undergoes spherical growth within the walls of the surrounding pore which is assumed to be a straight, vertical, cylindrical channel. Once the bubble diameter is equal to the pore diameter, the bubble continues to grow cylindrically. Bubble detachment occurs either due to nucleation of a new bubble or as a result of changes in the balance of drag, buoyancy, pressure, inertia and surface tension gradient forces. After detachment, the bubble travels through the pore to the interface of LGDL and flow channel. It then undergoes further spherical growth until it either coalesces with an adjacent bubble or detaches from the LGDL surface due to the drag forces exerted by the convective flow of water through the flow channel.

Li et al. [132] used optical high-speed imaging to observe the processes described theoretically by Nouri-Khorasani. They used a novel, thin LGDL with straight, cylindrical pores and observed spherical bubble growth along the wall of pores. This confirmed earlier findings that bubble nucleation occurs only along the triple-phase boundary (see Section 7) [57,62]. Due to this limitation, and the relatively large pore diameter in this work (100 μm), cylindrical growth and detachment from the LGDL surface were not observed. The authors also found increasing bubble detachment diameters from the catalyst surface for higher current density and temperature.

The detachment of bubbles from the LGDL surface has been visualized by neutron and X-ray imaging. Hoeh et al. [63] found rapid, sudden detachment of bubbles followed by a slow growth up to the

critical size. The location of detachment and bubble growth was observed to be constant, which implies the existence of preferential pathways through the LGDL. Leonard et al. [64] demonstrated the same periodicity of growth and detachment and further showed that detachment frequency and diameter increased with current density.

6 Mass Transport in the Membrane

The vast majority of commercial and experimental PEMWEs rely on Nafion as a proton-conducting membrane material, due to its high proton conductivity, chemical, and mechanical stability [133]. Therefore, the discussion in this section is limited to Nafion, even though many aspects of it can be transferred to other membrane materials.

Nafion is a perfluorinated sulfonic acid (PFSA) polymer membrane, comprised of a Teflon backbone that provides mechanical stability and hydrophilic sulfonate (SO_3^-) bearing perfluorovinyl ether side chains that form proton conducting domains. PFSA chemical structure is commonly expressed by equivalent weight (EW), the mass of dry membrane per mole of acid groups. Whilst poorly documented, Nafion polymer backbone lengths are on the order of 100 nm, with side chains roughly 0.8 nm long and regularly, but randomly distributed, approximately every 0.6−1.2 nm for Nafion with EW of 1100 g mol^{-1} [134]. Nafion morphology has been under investigation since its production and still remains elusive as a result of the random chemical structure being capable of organizing in a complex arrangement of ionic and crystalline domains with significant distribution in dimensions over a wide range of length scales. The current consensus describes ionic groups aggregated in the perfluorinated polymer matrix forming a network of clusters that allow for significant swelling by polar solvents, such as water, and facilitate ionic transport through these nanometre-scale domains. Many morphological models have been suggested based on various characterisation techniques (Figure 8), which are separated into cylindrical (Figure 8 (a)) and lamellar (Figure 8 (b)) structure models. While cylindrical models exhibit an unfavourable distribution of charge, with identical charges accumulating

in the centre of the pore, lamellar models cause a wider distribution of identical charge and an increased interaction of opposite charges.

The first model to be proposed was by Gierke et al. [135], with the 'cluster network model' (Figure 8 (g)), which is still popular today and is based on characterisation of the material via small- and wide-angle X-ray scattering (SAXS and WAXS). This model assumes Nafion to be composed of nano-phase separated ~4 nm diameter clusters of sulfonate-terminated side groups organised into inverted micelles. A contiguous network is formed via connecting 1 nm pores (or channels) lined by SO_3^- groups, within a semi-crystalline matrix, enabling inter-cluster transport of H^+ ions, but rejection of OH^- ions. Upon hydration, the spherical ionic clusters swell to accommodate the water by a combination of expansion in cluster size and redistribution of sulfonate sites, resulting in a reduced number of larger clusters [136].

The 'core-shell model' (Figure 8 (h)) was suggested after further SAXS and WAXD analysis by Fujimura et al. [137]. The observed structure was composed of an ion-rich core of sulfonated side groups, surrounded by an ion-poor shell, constructed mainly by perfluorocarbon chains [138]. These core-shell particles exist uniformly distributed in a matrix of fluorocarbon chains containing both, non-clustered ions and multiplets (intermediate ionic phase). This model has been developed into the parallel cylinder water channel model (Figure 8 (i)) by Schmidt-Rohr et al. [139], where the 'ionomer peak' is attributed to long parallel randomly packed water channels of 1.8 – 3.5 nm, surrounded by side branches forming inverted-micelle cylinders (Figure 8 (c)).

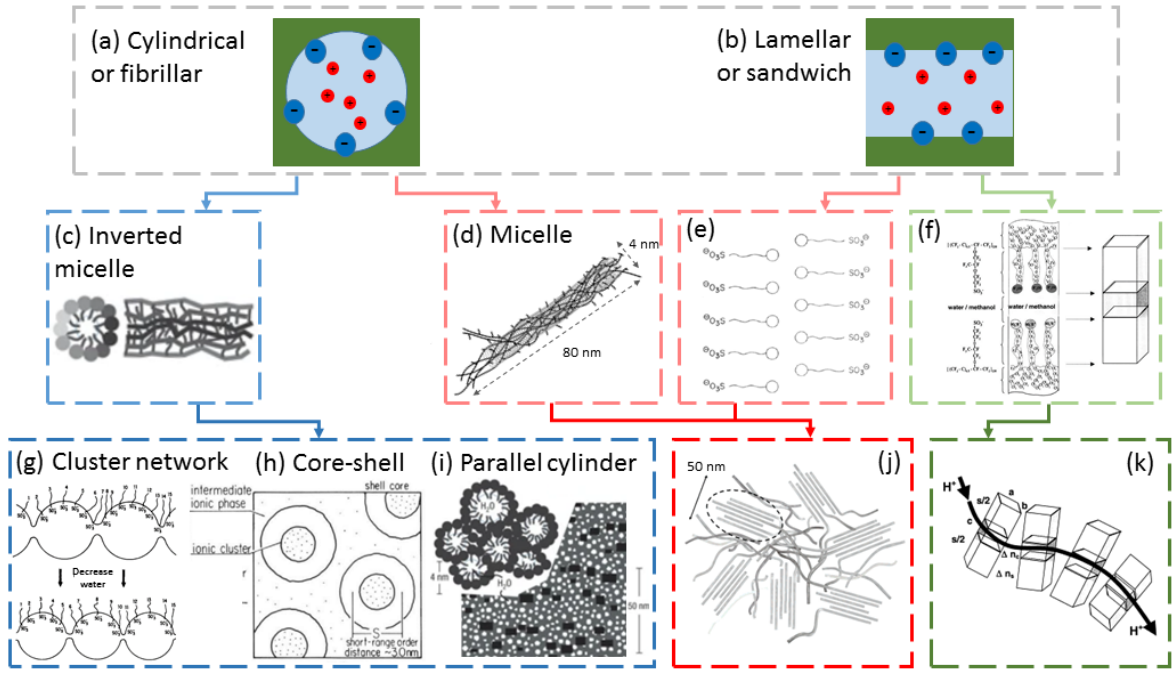

Fig.8: Nafion morphology at different length scales. The first row shows simplistic models of electrostatic interactions with **(a)** cylindrical pores and **(b)** a lamellar organisation. The second row shows the proposed models of nanoscale structure of aggregated polymer chains as **(c)** inverted micelles with side groups orientated inwards (seen side and face on) [139], **(d)** micelles with side groups orientated outwards and hydrophobic core forming fibres (or flat ribbons at low humidity) [140], **(e)** bilayer representation of crystallites with side groups extending on either side of polymer chains (aligned in plane with the page, shown as circles) [141], and **(f)** sandwich model [142]. The third row shows proposed macromolecular structures formed from the respective aggregate components as **(g)** a network of clusters [135], **(h)** core-shell model with dots indicating ionic sites [138], **(i)** inverted-micelle cylinders aligned into long parallel randomly packed water channels with crystallites (black oblongs) crosslinking for structural support [139], **(j)** bundles of orientated rod or ribbon like micellar aggregates connected by amorphous polymeric regions and contained in the water phase [140], **(k)** Randomly distributed sandwich structure elements forming cross-linked channels inside the membrane [142]. **(c)** and **(i):** Reprinted by permission from Springer Nature Customer Service Centre GmbH: Springer Nature, Nature Materials, Parallel cylindrical water nanochannels in Nafion fuel-cell membranes, Schmidt-Rohr et al., 2008, doi:10.1038/nmat2074. **(d)** and **(j):** Reprinted with permission from 'Rubatat et al., Macromolecules, 2004;37:7772–83'. Copyright (2004) American Chemical Society. **(e)**: Reprinted with permission from 'Starkweather HW, Macromolecules, 1982;15:320–3.'. Copyright (1982) American Chemical Society. **(f)** and **(k)**: Reprinted from 'Electrochimica Acta, 46, Haubold et al., Nano structure of NAFION: A SAXS study, 1559–63, 2001' with permission from Elsevier. **(g)**: Reprinted with permission from 'Gierke et al., J Polym Sci Part A-2, Polym Phys 1981;19:1687–704'. Copyright (1981) John Wiley and Sons. **(h)**: Reprinted with permission from 'Fujimura et al., Macromolecules 1982;15:136–44.'. Copyright (1982) American Chemical Society.

Recent experimental work has correlated the water content, polymer volume fractions and the ionomer peak present in Nafion [143], as well as observed fast structural reorganisation [144], to suggest the presence of a locally two-dimensional structure. This arrangement has been construed as 'lamellar' structures by Litt et al. [141,145] (Figure 8 (e)), 'sandwich-like' structures by Haubold et al. [142] (Figure 8 (f) and (k)), with shell region of polymer backbones and side-chains which orientate into the core region, and flat 'ribbons' (Figure 8 (d)) by Rubatat et al. [140,146] that coalesce to form 50–100 nm bundles heterogeneously distributed throughout the framework (Figure 8 (j)) [147].

The presence of lamellar like structures present within Nafion have been rationalised by preventing disadvantageous accumulation of positive and negative charges occurring in cylindrical water structures, but to date, no widely acknowledged unified theory of Nafion morphology exists. In depth understanding of the Nafion structure at all length scales is required to completely rationalise the dynamic process occurring within, such as water and proton transport.

6.1 Water Transport

Water is transported through the Nafion membrane via diffusion and electro-osmotic drag, while upon initial contact with water the membrane hydrates and swells, accompanied by internal structural reorganisation [148]. Therefore, hydration and swelling strongly affect water and proton transport as well as durability and physical properties of the membrane. Initial hydration of Nafion occurs by water binding to sulfonic acid groups, residing at the hydrophobic-hydrophilic interface, which gives an initial steeper increase of water uptake at low relative humidity (RH). This is followed by swelling due to the formation of bulk water within clusters at higher RH. The resulting fully hydrated Nafion has an average of 21 H_2O molecules per $–SO_3^-$-group [149,150]. However, it has been proposed that the hydrogen bonding between water molecules in fully hydrated Nafion is considerably less extensive than that in liquid water. This is likely due to the high surface-to-volume ratio in the narrow ionic domains causing a large population of H_2O molecules to reside at the hydrophobic-hydrophilic interfaces, especially if the polymer is irregularly structured [151].

At a low degree of hydration (7 wt%) the backbone motion is restricted by ion clustering. At higher water uptake (25 wt%) there is greater motion, suggesting a plasticizing effect of the water, likely caused by a weakening of the electrostatic interactions within clusters [152]. With no water molecules present, the side chains were predicted to be in a stiff folded conformation, whereas upon hydration the hydrophilic and flexible $–SO_3^-$-group, and possibly the ether group nearest the acid, had hydrogen bonding interactions with the water molecules [153].

It has also been shown that the hydration of the membrane affects the rate of water transport through the membrane. At high water activity within the membrane, fast water permeation occurs, making interfacial water transport the rate-limiting step. In a less hydrated Nafion membrane (low water activity), permeation is considerably slower and hence rate-limiting compared to interfacial transport [154,155]. It is not surprising that the values reported for the diffusion coefficient of water through Nafion vary widely [155].

The calculation of the water diffusion rate through the membrane in an operational PEMWE is based on Fick's law, which requires knowledge of the diffusion coefficient of water in Nafion. However, due to the very specific conditions in an operational PEMWE, the values obtained from permeation studies with Nafion cannot straightforwardly be applied. Therefore, modelling studies have used various approaches to obtain a value for the diffusion coefficient, such as adopting values [27] or correlations [156] from PEM fuel cell literature, or deploying correlations based on kinetic theory accounting for binary as well as Knudsen diffusion [25].

Besides diffusion, water molecules are also transported through the membrane along with protons migrating from anode to cathode, which is known as electro-osmotic drag. Details on calculating electro-osmotic drag can be found in Section 4.2. Furthermore, if a PEMWE is operated under differential pressure, water transport from cathode to anode occurs due to the pressure gradient and can be calculated according to Darcy's law [25,27,156].

6.2 Proton Transport

Proton mobility in water is abnormally high, with ion conductance around seven times that of Na^+ and five times that of K^+ at room temperature [157]. This is due to the sequence of proton-transfer reactions (hops) between water molecules in the Grotthuss mechanism [158]. Proton exchange membranes, such as Nafion, rely upon fundamental molecular events leading to proton transfer via structural reorganisation and diffusion within extended hydration structures.

The total proton conductivity in hydrated Nafion is understood to be the result of three contributions:

- Bulk water conductivity via Grotthuss diffusion (Figure 9 (a))
- Bulk water conductivity via vehicular diffusion (Figure 9 (b))
- Domain surface conductivity via proton hopping (e.g. from one sulfonate group to the next) (Figure 9 (c))

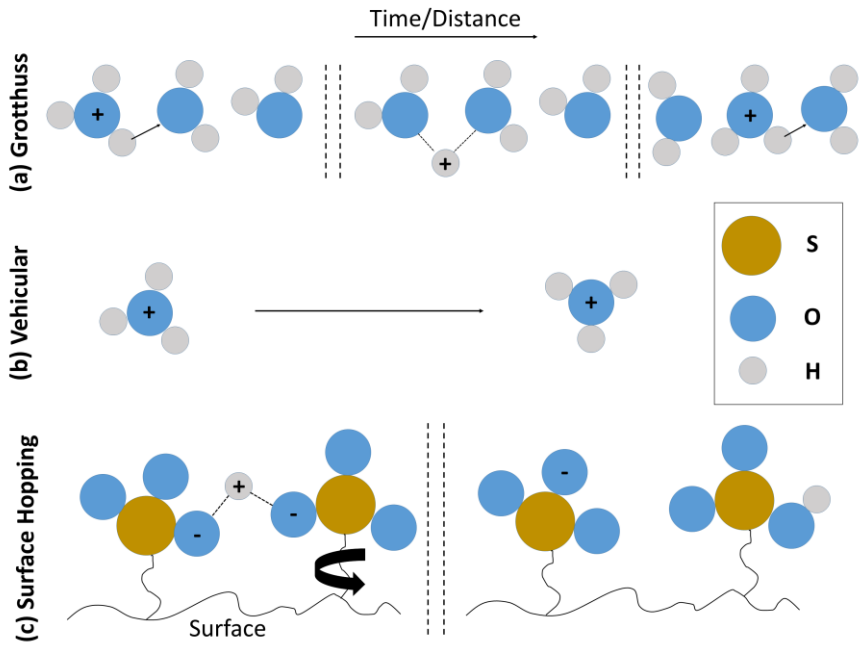

Fig. 9: The mechanisms of proton transport through Nafion. **(a)** The Grotthuss mechanism relies on the formation of hydrogen bonds between the proton and subsequent water molecules, while **(b)** the vehicular mechanism is equivalent to the transport of a hydronium ion. **(c)** Surface hopping is analogous to the Grotthuss mechanism, but occurs along the pore surface with the sulfonate group being the electron donor for the hydrogen bond.

Bulk Grotthuss diffusion is the dominant contributor to the total conductivity [159], occurring predominantly in the central region of the ionic domain (away from the walls). In the vehicular mechanism, the proton diffuses with a vehicle (H_3O^+), with the non-protonated vehicle (H_2O) diffusing in the opposite direction, resulting in a net transport of protons [160]. The contributions from Grotthuss and vehicular diffusion depend on temperature, pressure, frequency of proton hopping via hydrogen bonds, the rotational speed of carriers and diffusion coefficient [160].

Contribution of different mechanisms is also dependent on hydration state. At low hydration, Nafion $SO_3^{-}\cdots H^+OH_2$ groupings occur with H^+ biased towards the water molecule [161], and when $H_2O/SO_3H > 2$, the excess protons exist in water hydrogen bonds instead of acid-water hydrogen bonds. The mechanism for proton hopping along the negatively charged surface has a significantly higher activation energy due to electrostatic attraction between the two entities. Thus, this mechanism does not contribute significantly to the overall conductivity of protons, except at low water levels where it is the dominant mechanism, due to the water hydrogen bonding to the sulfonate groups. This proton transfer being two orders of magnitude slower is one of the reasons for low proton conductivity at low water content [162]. In addition, nearer the domain walls, water is increasingly more bound, therefore conductivity via the Grotthus and vehicular mechanisms decreases with hydration as the water phase decreases in size [163]. The balance between diffusion along the surface and through the bulk of the pore depends on the surface density of sulfonate groups and pore size, which can vary between specific PFSA and EW.

There are several other ionic species besides H_3O^+, which can also facilitate proton transport via vehicular or Grotthuss transport, namely hydrogen-bonding between two water molecules of an $H_5O_2^+$ grouping, and the Eigen $H_9O_4^+$ cluster with a H_3O^+ ion bonded to three H_2O molecules via the three protons of the H_3O^+. The presence of ions means the hydrogen bonds in these groupings are 1-2 orders more polarizable than in regular H_2O molecules, leading to the high proton conductivity. These clusters are linked to other H_2O molecules or SO_3^- acceptor groups. This facilitates proton migration over larger distances when these groupings shift within the extended hydration network

by thermal rearrangement [164]. The proton can rapidly transfer within one of the above structures to one of the outer H atoms of another molecule or cluster, and another H^+ transfer can take place with a third adjacent H_2O molecule. Thermal rearrangement causes $H_5O_2^+$ groupings to become redefined, 'structural diffusion', the rate-determining step. This proton conductivity is a cooperative process between the coupled H^+ motion within the extended hydration environment, which is what leads to the transport of protons from anode to cathode [165].

In conclusion, the proton conductivity depends on the porosity, volume fraction of absorbed water, tortuosity, proton concentration in the surface and bulk, and finally diffusion coefficients for the surface, Grotthuss, and vehicular mechanisms.

7 Mass Transport Diagnostic Techniques

There is a wide range of diagnostic techniques applied in the field of PEMWEs (Figure 10), these include the following:

- Electrochemical impedance spectroscopy (EIS) [166,167]
- Neutron imaging [65–69,168–170]
- X-ray imaging [63,171–174]
- Optical imaging [50,56,59–61]
- Porous transport layer (PTL)-on-a-chip [175,176]
- Acoustic techniques [71,177,178]

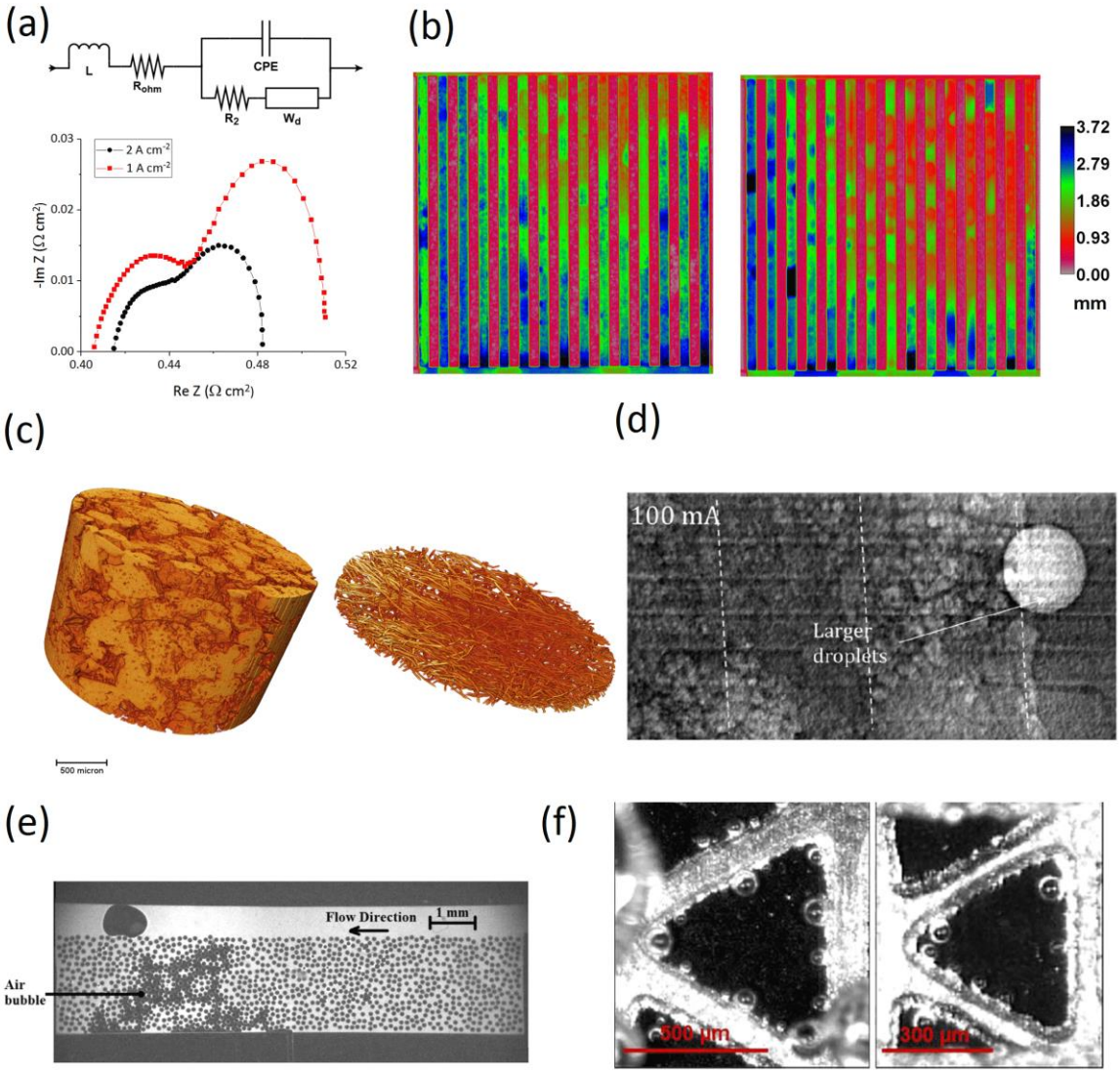

Fig. 10: Examples of commonly used diagnostic techniques: (a) Nyquist diagram produced from electrochemical impedance spectroscopy and an equivalent circuit, (b) through-plane water thickness measurement via neutron radiography, (c) X-ray computed tomography of a sintered and a fibrous LGDL material, (d) X-ray synchrotron radiography of channel and land areas in a PEMWE [64] (Reprinted from 'Electrochimica Acta, 276, Leonard et al., Operando X-ray tomography and sub-second radiography for characterizing transport in polymer electrolyte membrane electrolyzer, 424–33, 2018' with permission from Elsevier), (e) image obtained during a PTL-on-a-chip experiment [175] (Reprinted from 'J Power Sources, 258, Arbabi et al., Feasibility study of using microfluidic platforms for visualizing bubble flows in electrolyzer gas diffusion layers, 142–9, 2014' with permission from Elsevier), and (f) high-speed optical imaging of bubble nucleation along the triple-phase boundary of catalyst, LGDL, and water [60] (Reprinted with permission under a CC BY-NC licence (https://creativecommons.org/licenses/by-nc/4.0/legalcode) from 'Mo et al., Sci Adv 2016;2:e1600690–e1600690, https://advances.sciencemag.org/content/2/11/e1600690'. Copyright (2016) American Association for the Advancement of Science).

7.1 EIS

Electrochemical impedance spectroscopy (Figure 10 (a)) is commonly used to identify different voltage contributions (ohmic, activation, mass transport) to the overall performance of PEMWEs. Data analysis can be either qualitative by comparing EIS spectra at various conditions or quantitative by fitting the spectra to an equivalent electrical circuit and extracting values for the resistance and impedance elements. The exact form of the equivalent circuit and the number of elements in it varies widely [55,57,120,167,179–182] or is not reported at all. A more systematic approach to the analysis of EIS spectra, comparable to established work for fuel cells [183–186], has not yet been reported for PEMWEs.

Due to its versatility and comparable ease of application, the use of EIS is widespread. Examples include measuring the performance contribution of LGDLs [57], the effect of low platinum loadings on the cathode [187], localized performance [75], the effect of flow plate geometry [54], the role of LGDL microstructure [188], benchmark characterisation [94], the effect of water starvation [43] and intermittent operation [189], or the influence of flow effects on performance [55].

7.2 Neutron Imaging

The high sensitivity of neutrons towards hydrogen and water makes neutron imaging a powerful tool for the investigation of flow and mass transport phenomena in PEMWEs and PEM fuel cells [70] (Figure 10 (b)). *Operando* neutron imaging of a PEMWE was first demonstrated by Selamet et al. [65,168], while Hoeh et al. [66] used neutron imaging to measure the water-gas ratio under land and channel areas of a PEMWE.

Several examples demonstrate the level of insight into water saturation and movement in the LGDL that neutron imaging can offer. Seweryn et al. [68] found that the amount of water within the LGDL on the anode side is constant for current densities from 0.1 A cm^{-2} to 2.5 A cm^{-2}, which shows the ability of sintered titanium materials to hold up and transport large amounts of water and hence

prevent water starvation. Panchenko et al. compared the water content of a sintered titanium LGDL with a felt material used as LGDL [67] and found that 37 % of pore volume in a sintered LGDL did not contribute to mass transport while only water was flowing through the PEMWE (15 % during air flow only) [169]. Maier et al. [69] used neutron imaging and X-ray computed tomography to calculate water saturation and residence time in the LGDL and showed a heterogeneous water distribution across the active area, which is suggested to be linked to the non-uniform water flow distribution in the flow channels. Lee et al. [170] combined neutron radiography and electrochemical testing and found a decrease in mass transport overpotential at increased temperatures. This was assigned to a more uniform water-gas distribution in the flow channels, due to the reduced viscosity of water at high temperatures.

7.3 X-ray Imaging

Whilst X-rays lack the high sensitivity of neutrons towards water, the extremely high flux of synchrotron sources allows for very short exposure times (sub-second radiography). Synchrotron X-ray imaging (Figure 10 (d)) was first used by Hoeh et al. [63] for imaging of a PEMWE *operando*. The authors showed the periodicity of bubble formation and detachment at specific locations on the surface of the LGDL, supporting the theory of preferential pathways for mass transport. While the work of Hoeh et al. was limited to radiography, Leonard et al. [64] obtained three-dimensional tomography data sets during operation of a PEMWE. This allowed the authors to study a multitude of processes on different length scales, ranging from catalyst thinning and redeposition to the formation of bubbles and their movement in the flow channels.

Besides synchrotron *operando* imaging of whole PEMWEs, the use of lab-scale X-ray sources for micro-computed tomography (X-ray CT) has been prolific in recent years. X-ray CT allows for the in-depth study of the microstructure of LGDL materials *ex-situ* and can achieve a spatial resolution in the range of a few micrometres (Figure 10 (c)). Several authors have combined X-ray CT with EIS and electrochemical characterisation to link LGDL microstructure and performance

[120,167,188,190,191]. XCT data can further be used to calculate various transport properties like thermal and electrical conductivity and permeability [172].

7.4 Optical Imaging

The investigation of flow phenomena via high-speed optical imaging is limited to macroscopic spatial resolution of optically accessible processes occurring in optically accessible regions, such as the flow channels or open pores of perforated plates. However, it is a low-cost, easy to implement and therefore widespread diagnostic tool. It is often used in conjunction with electrochemical characterization techniques, such as i-V-curves or EIS (Figure 10 (f)).

Optical imaging has proven very valuable when observing bubble nucleation in the pores of perforated plates, allowing direct optical access to the interface between catalyst layer and LGDL [57,62,132,192]. It has been shown that bubble nucleation only occurs along the pore edge, not in its centre, as visible in (Figure 10 (f)) [60]. This is due to the fact that catalytic active sites on the CCM, the current conduction through the LGDL, and water exist in close proximity only on the pore edge, while electrons have to travel along the surface of the CCM to reach catalyst sites further towards the middle of the pore. In order to examine the role of in-plane resistivity further a numerical model was developed and used to simulate the current distribution within one pore as well as the overall performance of a PEMWE with LGDLs of different pore sizes and porosities [193].

Based on the new insight from the optical imaging experiments, a novel concept for PEMWEs in which the catalyst is only applied along the edges of the LGDL pores on the membrane site has been proposed [60], which allows for a much higher catalyst utilization. In an attempt to examine the impact of catalyst reduction, Kang et al. [58] sputter-coated a thin LGDL with straight pores and a porosity of 50 % with platinum. They showed that the use of this system does not reduce performance compared to using a conventional CCM, while the catalyst utilization was improved by a factor of around 30. Further, Mo et al. [61] developed a LGDL with an additional metal rod through the diameter of a pore

in a perforated plate. They used optical imaging to prove catalytic activity around the surface of the rod and the consequential improvement in catalyst utilization.

Dedigama et al. used optical imaging in combination with EIS and localized current density measurements, which allowed for a correlation of flow regime to local and overall performance. The authors found a performance improvement in slug flow, which they attributed to more efficient bubble removal from the surface of the LGDL [55,56].

Lafmejani et al. simulated the environment on the anode side of a PEMWE by passing gas through different LGDL materials while flowing water over its surface. They used optical imaging to observe the locations of bubble formation, the development of the flow regime and flow patterns along the length of the LGDL [76,78,194].

7.5 PTL-on-a-Chip

An interesting approach to analysing mass transport within a porous LGDL is the so-called porous transport layer (PTL)-on-a-Chip (Figure 10 (e)). The authors created a 2D representation of different LGDL materials and analysed the flow of water and gas through this layer using optical microscopy [175,176]. This allows for the visualization of exact pathways of gas through the material which are usually obstructed by the thickness of the LGDL. Using this technique, Lee et al. [176] found that the bubble growth within pores of the LGDL consists of two different steps. During pressurization the bubble is stationary and its size constant while its internal pressure is increasing. Once the pressure reaches a critical value, the penetration step follows and the bubble rapidly expands into a neighbouring pore. The dynamics of this process are controlled by the diameter of the throat between the pores. As a consequence, within the pathway of gas through the LGDL, a limiting throat size exists, to penetrate which the highest internal pressure is necessary. Once this limiting throat size is passed, breakthrough to the surface of the LGDL immediately occurs. These findings shed new light on a number of studies examining the influence of LGDL pore size on PEMWE performance [72,73,95]. It is expected that throat size correlates quite closely to pore size, so the influence of pore size on

performance found in these studies is likely to be related to the throat size effect described above. Qualitative findings from PTL-on-a-chip experiments are well suited to inform further pore network and modelling studies [195].

8 Conclusion

The importance of mass transfer aspects in PEMWEs is increasingly acknowledged in the scientific literature. This review attempts to describe the sources of mass transfer limitation and provide a framework for understanding the growing literature associated with this topic. The role of PEMWEs in the Hydrogen Economy and as a means for energy grid stabilization is outlined in the Introduction and the further sections provide insights into mass transport in the flow channels, LGDL, and membrane of PEMWEs.

The mass transport in the flow channels has been discussed, including different flow regimes, flow-field geometries, and the calculation of the relevant mass flows. Further, the most commonly used LGDL materials, their properties, as well as surface and structural modifications proposed in literature to address mass transport limitations, are outlined. After a discussion of water and proton transport in the polymer electrolyte membrane, this work concludes by outlining a range of different diagnostic techniques used to analyse PEMWE mass transport processes.

Four aspects of special relevance shall be mentioned here, each still awaiting a conclusive answer:

- The effect of the flow regime in the flow channels on the overall PEMWE performance is still unclear. Intelligent experimental design will be required to isolate this effect from other parameters and deliver an unequivocal conclusion.
- A comprehensive analytical solution to describe the flux of water and gas and the appropriate transport mechanism(s) through the LGDL is yet to be formulated.

- Various materials are commonly used as LGDLs for PEMWEs. A definitive answer on which materials work best in which set of conditions is still not found, and the development of advanced LGDL materials and architectures is required.
- The exact morphological structure of Nafion at varying stages of hydration has yet to be fully described, potentially unifying the already existing models and contradictory experimental evidence. The properties of Nafion in its fully hydrated state are particularly relevant for PEMWEs.

Acknowledgements

The authors acknowledge financial support into the EIL's hydrogen, electrolyser and fuel cell activity from the EPSRC through grants (EP/R023581/1; EP/P009050/1; EP/N032888/1; EP/M014371/1; EP/M009394; EP/L015749/1; EP/K038656/1). Support from the National Measurement System of the UK's Department of Business, Energy & Industrial Strategy is also gratefully acknowledged. PRS acknowledges funding from The Royal Academy of Engineering (CiET1718/59).

References

[1] J.O.M. Bockris, The hydrogen economy: Its history, Int. J. Hydrogen Energy. 38 (2013) 2579–2588. doi:10.1016/j.ijhydene.2012.12.026.

[2] G. Marbán, T. Valdés-Solís, Towards the hydrogen economy?, Int. J. Hydrogen Energy. 32 (2007) 1625–1637. doi:10.1016/j.ijhydene.2006.12.017.

[3] S. Sharma, S.K. Ghoshal, Hydrogen the future transportation fuel: From production to applications, Renew. Sustain. Energy Rev. 43 (2015) 1151–1158. doi:10.1016/j.rser.2014.11.093.

[4] G.W. Crabtree, M.S. Dresselhaus, M. V Buchanan, The Hydrogen Economy, Phys. Today. (2004) 39–45. doi:10.1063/1.1878333.

[5] J.D. Holladay, J. Hu, D.L. King, Y. Wang, An overview of hydrogen production technologies,

Catal. Today. 139 (2009) 244–260. doi:10.1016/j.cattod.2008.08.039.

[6] T. da Silva Veras, T.S. Mozer, D. da Costa Rubim Messeder dos Santos, A. da Silva César, Hydrogen: Trends, production and characterization of the main process worldwide, Int. J. Hydrogen Energy. 42 (2017) 2018–2033. doi:10.1016/j.ijhydene.2016.08.219.

[7] R. Bhandari, C.A. Trudewind, P. Zapp, Life cycle assessment of hydrogen production via electrolysis - A review, J. Clean. Prod. 85 (2014) 151–163. doi:10.1016/j.jclepro.2013.07.048.

[8] I. Dincer, C. Acar, Review and evaluation of hydrogen production methods for better sustainability, Int. J. Hydrogen Energy. 40 (2014) 11094–11111. doi:10.1016/j.ijhydene.2014.12.035.

[9] J. Turner, G. Sverdrup, M.K. Mann, P.-C. Maness, B. Kroposki, M. Ghirardi, R.J. Evans, D. Blake, Renewable hydrogen production, Int. J. Energy Res. 32 (2008) 379–407. doi:10.1002/er.

[10] A. Buttler, H. Spliethoff, Current status of water electrolysis for energy storage, grid balancing and sector coupling via power-to-gas and power-to-liquids: A review, Renew. Sustain. Energy Rev. 82 (2018) 2440–2454. doi:10.1016/j.rser.2017.09.003.

[11] M. Carmo, D.L. Fritz, J. Mergel, D. Stolten, A comprehensive review on PEM water electrolysis, Int. J. Hydrogen Energy. 38 (2013) 4901–4934. doi:10.1016/j.ijhydene.2013.01.151.

[12] A. Villagra, P. Millet, An analysis of PEM water electrolysis cells operating at elevated current densities, Int. J. Hydrogen Energy. 44 (2019) 9708–9717. doi:10.1016/j.ijhydene.2018.11.179.

[13] M. Kopp, D. Coleman, C. Stiller, K. Scheffer, J. Aichinger, B. Scheppat, Energiepark Mainz: Technical and economic analysis of the worldwide largest Power-to-Gas plant with PEM electrolysis, Int. J. Hydrogen Energy. 42 (2017) 13311–13320. doi:10.1016/j.ijhydene.2016.12.145.

[14] P. Aßmann, A.S. Gago, P. Gazdzicki, K.A. Friedrich, M. Wark, Toward developing accelerated stress tests for proton exchange membrane electrolyzers, Curr. Opin. Electrochem. 21 (2020)

225–233. doi:10.1016/j.coelec.2020.02.024.

[15] S.M. Saba, M. Müller, M. Robinius, D. Stolten, The investment costs of electrolysis – A comparison of cost studies from the past 30 years, Int. J. Hydrogen Energy. 43 (2018) 1209–1223. doi:10.1016/j.ijhydene.2017.11.115.

[16] L. Allidières, A. Brisse, P. Millet, S. Valentin, M. Zeller, On the ability of pem water electrolysers to provide power grid services, Int. J. Hydrogen Energy. 44 (2019) 9690–9700. doi:10.1016/j.ijhydene.2018.11.186.

[17] L. Bertuccioli, A. Chan, D. Hart, F. Lehner, B. Madden, E. Standen, Study on development of water electrolysis in the EU, 2014.

[18] M. Bühler, P. Holzapfel, D. McLaughlin, S. Thiele, From catalyst coated membranes to porous transport electrode based configurations in PEM water electrolyzers, J. Electrochem. Soc. 166 (2019) F1070–F1078. doi:10.1149/2.0581914jes.

[19] M. Bühler, F. Hegge, P. Holzapfel, M. Bierling, M. Suermann, S. Vierrath, S. Thiele, Optimization of anodic porous transport electrodes for proton exchange membrane water electrolyzers, J. Mater. Chem. A. 7 (2019) 26984–26995. doi:10.1039/c9ta08396k.

[20] Ö.F. Selamet, F. Becerikli, M.D. Mat, Y. Kaplan, Development and testing of a highly efficient proton exchange membrane (PEM) electrolyzer stack, Int. J. Hydrogen Energy. 36 (2011) 11480–11487. doi:10.1016/j.ijhydene.2011.01.129.

[21] K. Ayers, The potential of proton exchange membrane–based electrolysis technology, Curr. Opin. Electrochem. 18 (2019) 9–15. doi:10.1016/j.coelec.2019.08.008.

[22] G. Chisholm, P.J. Kitson, N.D. Kirkaldy, L.G. Bloor, L. Cronin, 3D printed flow plates for the electrolysis of water: an economic and adaptable approach to device manufacture, Energy Environ. Sci. 7 (2014) 3026–3032. doi:10.1039/C4EE01426J.

[23] G. Yang, J. Mo, Z. Kang, Y. Dohrmann, F.A. List, J.B. Green, S.S. Babu, F.Y. Zhang, Fully printed

and integrated electrolyzer cells with additive manufacturing for high-efficiency water splitting, Appl. Energy. 215 (2018) 202–210. doi:10.1016/j.apenergy.2018.02.001.

[24] M. Schalenbach, M. Carmo, D.L. Fritz, Pressurized PEM water electrolysis: Efficiency and gas crossover, Int. J. Hydrogen Energy. 38 (2013) 14921–14933. doi:10.1016/j.ijhydene.2013.09.013.

[25] Z. Abdin, C.J. Webb, E.M. Gray, Modelling and simulation of a proton exchange membrane (PEM) electrolyser cell, Int. J. Hydrogen Energy. 40 (2015) 13243–13257. doi:10.1016/j.ijhydene.2015.07.129.

[26] B. Han, J. Mo, Z. Kang, G. Yang, W. Barnhill, F.Y. Zhang, Modeling of two-phase transport in proton exchange membrane electrolyzer cells for hydrogen energy, Int. J. Hydrogen Energy. 42 (2017) 4478–4489. doi:10.1016/j.ijhydene.2016.12.103.

[27] F. Marangio, M. Santarelli, M. Calì, Theoretical model and experimental analysis of a high pressure PEM water electrolyser for hydrogen production, Int. J. Hydrogen Energy. 34 (2009) 1143–1158. doi:10.1016/j.ijhydene.2008.11.083.

[28] F.Z. Aouali, M. Becherif, H.S. Ramadan, M. Emziane, A. Khellaf, K. Mohammedi, Analytical modelling and experimental validation of proton exchange membrane electrolyser for hydrogen production, Int. J. Hydrogen Energy. 42 (2017) 1366–1374. doi:10.1016/j.ijhydene.2016.03.101.

[29] A. Awasthi, K. Scott, S. Basu, Dynamic modeling and simulation of a proton exchange membrane electrolyzer for hydrogen production, Int. J. Hydrogen Energy. 36 (2011) 14779–14786. doi:10.1016/j.ijhydene.2011.03.045.

[30] H. Kim, M. Park, K.S. Lee, One-dimensional dynamic modeling of a high-pressure water electrolysis system for hydrogen production, Int. J. Hydrogen Energy. 38 (2013) 2596–2609. doi:10.1016/j.ijhydene.2012.12.006.

[31] S. Toghyani, E. Afshari, E. Baniasadi, S.A. Atyabi, Thermal and electrochemical analysis of different flow field patterns in a PEM electrolyzer, Electrochim. Acta. 267 (2018) 234–245. doi:10.1016/j.electacta.2018.02.078.

[32] R. García-Valverde, N. Espinosa, A. Urbina, Simple PEM water electrolyser model and experimental validation, Int. J. Hydrogen Energy. 37 (2012) 1927–1938. doi:10.1016/j.ijhydene.2011.09.027.

[33] Z.H. Wang, C.Y. Wang, K.S. Chen, Two-phase flow and transport in the air cathode of proton exchange membrane fuel cells, J. Power Sources. 94 (2001) 40–50. doi:10.1016/S0378-7753(00)00662-5.

[34] E.J.F. Dickinson, A.J. Wain, The Butler-Volmer equation in electrochemical theory: Origins, value, and practical application, J. Electroanal. Chem. 872 (2020) 114145. doi:10.1016/j.jelechem.2020.114145.

[35] S. Toghyani, S. Fakhradini, E. Afshari, E. Baniasadi, M.Y. Abdollahzadeh Jamalabadi, M. Safdari Shadloo, Optimization of operating parameters of a polymer exchange membrane electrolyzer, Int. J. Hydrogen Energy. 44 (2019) 6403–6414. doi:10.1016/j.ijhydene.2019.01.186.

[36] B. Han, S.M. Steen, J. Mo, F.Y. Zhang, Electrochemical performance modeling of a proton exchange membrane electrolyzer cell for hydrogen energy, Int. J. Hydrogen Energy. 40 (2015) 7006–7016. doi:10.1016/j.ijhydene.2015.03.164.

[37] B. Han, J. Mo, Z. Kang, F.Y. Zhang, Effects of membrane electrode assembly properties on two-phase transport and performance in proton exchange membrane electrolyzer cells, Electrochim. Acta. 188 (2016) 317–326. doi:10.1016/j.electacta.2015.11.139.

[38] G. Yang, S. Yu, J. Mo, Z. Kang, Y. Dohrmann, F.A. List, J.B. Green, S.S. Babu, F.Y. Zhang, Bipolar plate development with additive manufacturing and protective coating for durable and high-efficiency hydrogen production, J. Power Sources. 396 (2018) 590–598.

doi:10.1016/j.jpowsour.2018.06.078.

[39] K. Mishima, T. Hibiki, Some characteristics of air-water two-phase flow in small diameter vertical tubes, Int. J. Multiph. Flow. 22 (1996) 703–712. doi:10.1016/0301-9322(96)00010-9.

[40] H. Ito, T. Maeda, A. Nakano, Y. Hasegawa, N. Yokoi, C.M. Hwang, M. Ishida, A. Kato, T. Yoshida, Effect of flow regime of circulating water on a proton exchange membrane electrolyzer, Int. J. Hydrogen Energy. 35 (2010) 9550–9560. doi:10.1016/j.ijhydene.2010.06.103.

[41] K. Onda, T. Murakami, T. Hikosaka, M. Kobayashi, R. Notu, K. Ito, Performance Analysis of Polymer-Electrolyte Water Electrolysis Cell at a Small-Unit Test Cell and Performance Prediction of Large Stacked Cell, J. Electrochem. Soc. 149 (2002) A1069. doi:10.1149/1.1492287.

[42] E. Afshari, S. Khodabakhsh, N. Jahantigh, S. Toghyani, Performance assessment of gas crossover phenomenon and water transport mechanism in high pressure PEM electrolyzer, Int. J. Hydrogen Energy. 46 (2021) 11029–11040. doi:10.1016/j.ijhydene.2020.10.180.

[43] S. Sun, Y. Xiao, D. Liang, Z. Shao, H. Yu, M. Hou, B. Yi, Behaviors of a proton exchange membrane electrolyzer under water starvation, RSC Adv. 5 (2015) 14506–14513. doi:10.1039/C4RA14104K.

[44] T. Cubaud, C.M. Ho, Transport of bubbles in square microchannels, Phys. Fluids. 16 (2004) 4575–4585. doi:10.1063/1.1813871.

[45] A.C. Olesen, S.H. Frensch, S.K. Kær, Towards uniformly distributed heat, mass and charge: A flow field design study for high pressure and high current density operation of PEM electrolysis cells, Electrochim. Acta. 293 (2019) 476–495. doi:10.1016/j.electacta.2018.10.008.

[46] A. Christian, C. Rømer, S. Knudsen, A numerical study of the gas-liquid , two-phase flow maldistribution in the anode of a high pressure PEM water electrolysis cell, Int. J. Hydrogen Energy. 41 (2015) 52–68. doi:10.1016/j.ijhydene.2015.09.140.

[47] S.S. Lafmejani, A.C. Olesen, S.K. Kær, VOF modelling of gas–liquid flow in PEM water electrolysis cell micro-channels, Int. J. Hydrogen Energy. 42 (2017) 16333–16344. doi:10.1016/j.ijhydene.2017.05.079.

[48] C. Minnaar, F. De Beer, D. Bessarabov, Current Density Distribution of Electrolyzer Flow Fields: In Situ Current Mapping and Neutron Radiography, Energy and Fuels. 34 (2020) 1014–1023. doi:10.1021/acs.energyfuels.9b03814.

[49] J. Nie, Y. Chen, S. Cohen, B.D. Carter, R.F. Boehm, Numerical and experimental study of three-dimensional fluid flow in the bipolar plate of a PEM electrolysis cell, Int. J. Therm. Sci. 48 (2009) 1914–1922. doi:10.1016/j.ijthermalsci.2009.02.017.

[50] J.O. Majasan, J.I.S. Cho, I. Dedigama, D. Tsaoulidis, P. Shearing, D.J.L. Brett, Two-phase flow behaviour and performance of polymer electrolyte membrane electrolysers: Electrochemical and optical characterisation, Int. J. Hydrogen Energy. 43 (2018) 15659–15672. doi:10.1016/j.ijhydene.2018.07.003.

[51] H. Li, H. Nakajima, A. Inada, K. Ito, Effect of flow-field pattern and flow configuration on the performance of a polymer-electrolyte-membrane water electrolyzer at high temperature, Int. J. Hydrogen Energy. 43 (2018) 8600–8610. doi:10.1016/j.ijhydene.2018.02.171.

[52] J. Wang, H. Wang, Discrete approach for flow field designs of parallel channel configurations in fuel cells, Int. J. Hydrogen Energy. 37 (2012) 10881–10897. doi:10.1016/j.ijhydene.2012.04.034.

[53] J. Wang, H. Wang, Flow-field designs of bipolar plates in PEM fuel cells: Theory and applications, Fuel Cells. 12 (2012) 989–1003. doi:10.1002/fuce.201200074.

[54] J.O. Majasan, J.I.S. Cho, M. Maier, I. Dedigama, P.R. Shearing, D.J.L. Brett, Effect of Anode Flow Channel Depth on the Performance of Polymer Electrolyte Membrane Water Electrolyser, ECS Trans. 85 (2018) 1593–1603. doi:10.1149/08513.1593ecst.

[55] I. Dedigama, P. Angeli, K. Ayers, J.B. Robinson, P.R. Shearing, D. Tsaoulidis, D.J.L. Brett, In situ diagnostic techniques for characterisation of polymer electrolyte membrane water electrolysers - Flow visualisation and electrochemical impedance spectroscopy, Int. J. Hydrogen Energy. 39 (2014) 4468–4482. doi:10.1016/j.ijhydene.2014.01.026.

[56] I. Dedigama, P. Angeli, N. Van Dijk, J. Millichamp, D. Tsaoulidis, P.R. Shearing, D.J.L. Brett, Current density mapping and optical flow visualisation of a polymer electrolyte membrane water electrolyser, J. Power Sources. 265 (2014) 97–103. doi:10.1016/j.jpowsour.2014.04.120.

[57] Z. Kang, J. Mo, G. Yang, S.T. Retterer, D.A. Cullen, T.J. Toops, J.B. Green Jr, M.M. Mench, F.-Y. Zhang, Investigation of thin/well-tunable liquid/gas diffusion layers exhibiting superior multifunctional performance in low-temperature electrolytic water splitting, Energy Environ. Sci. 10 (2017) 166–175. doi:10.1039/C6EE02368A.

[58] Z. Kang, G. Yang, J. Mo, Y. Li, S. Yu, D.A. Cullen, S.T. Retterer, T.J. Toops, G. Bender, B.S. Pivovar, J.B. Green, F.Y. Zhang, Novel thin/tunable gas diffusion electrodes with ultra-low catalyst loading for hydrogen evolution reactions in proton exchange membrane electrolyzer cells, Nano Energy. 47 (2018) 434–441. doi:10.1016/j.nanoen.2018.03.015.

[59] Z. Kang, G. Yang, J. Mo, S. Yu, D.A. Cullen, S.T. Retterer, T.J. Toops, M.P. Brady, G. Bender, B.S. Pivovar, J.B. Green, F.Y. Zhang, Developing titanium micro/nano porous layers on planar thin/tunable LGDLs for high-efficiency hydrogen production, Int. J. Hydrogen Energy. 43 (2018) 14618–14628. doi:10.1016/j.ijhydene.2018.05.139.

[60] J. Mo, Z. Kang, S.T. Retterer, D.A. Cullen, T.J. Toops, J.B. Green, M.M. Mench, F.-Y. Zhang, Discovery of true electrochemical reactions for ultrahigh catalyst mass activity in water splitting, Sci. Adv. 2 (2016) e1600690–e1600690. doi:10.1126/sciadv.1600690.

[61] J. Mo, Z. Kang, G. Yang, Y. Li, S.T. Retterer, D.A. Cullen, T.J. Toops, G. Bender, B.S. Pivovar, J.B. Green, F.Y. Zhang, In situ investigation on ultrafast oxygen evolution reactions of water splitting in proton exchange membrane electrolyzer cells, J. Mater. Chem. A. 5 (2017) 18469–18475.

doi:10.1039/c7ta05681h.

[62] J. Mo, Z. Kang, G. Yang, D. Talley, Visualization on Rapid and Micro-Scale Dynamics of Oxygen Bubble Evolution in PEMECs, in: Proc. 12th IEEE Int. Conf. Nano/Micro Eng. Mol. Syst., Los Angeles, 2017: pp. 101–105.

[63] M.A. Hoeh, T. Arlt, I. Manke, J. Banhart, D.L. Fritz, W. Maier, W. Lehnert, In operando synchrotron X-ray radiography studies of polymer electrolyte membrane water electrolyzers, Electrochem. Commun. 55 (2015) 55–59. doi:10.1016/j.elecom.2015.03.009.

[64] E. Leonard, A.D. Shum, S. Normile, D.C. Sabarirajan, D.G. Yared, X. Xiao, I. V Zenyuk, Operando X-ray tomography and sub-second radiography for characterizing transport in polymer electrolyte membrane electrolyzer, Electrochim. Acta. 276 (2018) 424–433. doi:10.1016/j.electacta.2018.04.144.

[65] O.F. Selamet, U. Pasaogullari, D. Spernjak, D.S. Hussey, D.L. Jacobson, M.D. Mat, Two-phase flow in a proton exchange membrane electrolyzer visualized in situ by simultaneous neutron radiography and optical imaging, Int. J. Hydrogen Energy. 38 (2013) 5823–5835. doi:10.1016/j.ijhydene.2013.02.087.

[66] M.A. Hoeh, T. Arlt, N. Kardjilov, I. Manke, J. Banhart, D.L. Fritz, J. Ehlert, W. Lüke, W. Lehnert, In-operando Neutron Radiography Studies of Polymer Electrolyte Membrane Water Electrolyzers, ECS Trans. 69 (2015) 1135–1140.

[67] O. Panchenko, E. Borgardt, W. Zwaygardt, F.J. Hackemüller, M. Bram, N. Kardjilov, T. Arlt, I. Manke, M. Müller, D. Stolten, W. Lehnert, In-situ two-phase flow investigation of different porous transport layer for a polymer electrolyte membrane (PEM) electrolyzer with neutron spectroscopy, J. Power Sources. 390 (2018) 108–115. doi:10.1016/j.jpowsour.2018.04.044.

[68] J. Seweryn, J. Biesdorf, T.J. Schmidt, P. Boillat, Communication—Neutron Radiography of the Water/Gas Distribution in the Porous Layers of an Operating Electrolyser, J. Electrochem. Soc.

163 (2016) F3009–F3011. doi:10.1149/2.0641607jes.

[69] M. Maier, J. Dodwell, R. Ziesche, C. Tan, T. Heenan, J. Majasan, N. Kardjilov, H. Markötter, I. Manke, L. Castanheira, G. Hinds, P.R. Shearing, D.J.L. Brett, Mass transport in polymer electrolyte membrane water electrolyser liquid-gas diffusion layers: A combined neutron imaging and X-ray computed tomography study, J. Power Sources. 455 (2020). doi:10.1016/j.jpowsour.2020.227968.

[70] N. Kardjilov, I. Manke, R. Woracek, A. Hilger, J. Banhart, Advances in neutron imaging, Mater. Today. 21 (2018) 652–672. doi:10.1016/j.mattod.2018.03.001.

[71] M. Maier, Q. Meyer, J. Majasan, C. Tan, I. Dedigama, J. Robinson, J. Dodwell, Y. Wu, L. Castanheira, G. Hinds, P.R. Shearing, D.J.L. Brett, Operando flow regime diagnosis using acoustic emission in a polymer electrolyte membrane water electrolyser, J. Power Sources. 424 (2019) 138–149. doi:10.1016/j.jpowsour.2019.03.061.

[72] H. Ito, T. Maeda, A. Nakano, C.M. Hwang, M. Ishida, A. Kato, T. Yoshida, Experimental study on porous current collectors of PEM electrolyzers, Int. J. Hydrogen Energy. 37 (2012) 7418–7428. doi:10.1016/j.ijhydene.2012.01.095.

[73] H. Ito, T. Maeda, A. Nakano, A. Kato, T. Yoshida, Influence of pore structural properties of current collectors on the performance of proton exchange membrane electrolyzer, Electrochim. Acta. 100 (2013) 242–248. doi:10.1016/j.electacta.2012.05.068.

[74] C. Immerz, M. Schweins, P. Trinke, B. Bensmann, M. Paidar, T. Bystroň, K. Bouzek, R. Hanke-Rauschenbach, Experimental characterization of inhomogeneity in current density and temperature distribution along a single-channel PEM water electrolysis cell, Electrochim. Acta. 260 (2018) 582–588. doi:10.1016/j.electacta.2017.12.087.

[75] C. Immerz, B. Bensmann, P. Trinke, M. Suermann, R. Hanke-Rauschenbach, Local current density and electrochemical impedance measurements within 50 cm single-channel PEM

electrolysis cell, J. Electrochem. Soc. 165 (2018) F1292–F1299. doi:10.1149/2.0411816jes.

[76] S.S. Lafmejani, A.C. Olesen, S.A. Shakhshir, S.K. Kaer, Analysing Gas-Liquid Flow in PEM Electrolyser Micro-Channels using a Micro-Porous Ceramic as Gas Permeable wall, ECS Trans. 80 (2017) 1107–1115.

[77] J. Garcia-Navarro, M. Schulze, K.A. Friedrich, Understanding the Role of Water Flow and the Porous Transport Layer on the Performance of Proton Exchange Membrane Water Electrolyzers, ACS Sustain. Chem. Eng. 7 (2019) 1600–1610. doi:10.1021/acssuschemeng.8b05369.

[78] S.S. Lafmejani, M. Müller, A.C. Olesen, S.K. Kær, Experimental and numerical study of flow in expanded metal plate for water electrolysis applications, J. Power Sources. 397 (2018) 334–342. doi:10.1016/j.jpowsour.2018.07.032.

[79] F. Arbabi, H. Montazeri, R. Abouatallah, R. Wang, A. Bazylak, Three-dimensional computational fluid dynamics modelling of oxygen bubble transport in polymer electrolyte membrane electrolyzer porous transport layers, J. Electrochem. Soc. 163 (2016) F3062–F3069. doi:10.1149/2.0091611jes.

[80] M. Upadhyay, S. Lee, S. Jung, Y. Choi, S. Moon, H. Lim, Systematic assessment of the anode flow field hydrodynamics in a new circular PEM water electrolyser, Int. J. Hydrogen Energy. 45 (2020) 20765–20775. doi:10.1016/j.ijhydene.2020.05.164.

[81] S. Toghyani, E. Afshari, E. Baniasadi, Metal foams as flow distributors in comparison with serpentine and parallel flow fields in proton exchange membrane electrolyzer cells, Electrochim. Acta. 290 (2018) 506–519. doi:10.1016/j.electacta.2018.09.106.

[82] S. Toghyani, E. Afshari, E. Baniasadi, Three-dimensional computational fluid dynamics modeling of proton exchange membrane electrolyzer with new flow field pattern, J. Therm. Anal. Calorim. 135 (2019) 1911–1919. doi:10.1007/s10973-018-7236-5.

[83] F. Civan, Porous Media Transport Phenomena, Wiley, 2011. doi:10.1029/2003WR002800.Aziz.

[84] A. Zinser, G. Papakonstantinou, K. Sundmacher, Analysis of mass transport processes in the anodic porous transport layer in PEM water electrolysers, Int. J. Hydrogen Energy. 44 (2019) 28077–28087. doi:10.1016/j.ijhydene.2019.09.081.

[85] G. Schmidt, M. Suermann, B. Bensmann, R. Hanke-Rauschenbach, I. Neuweiler, Modeling Overpotentials Related to Mass Transport Through Porous Transport Layers of PEM Water Electrolysis Cells, J. Electrochem. Soc. 167 (2020) 114511. doi:10.1149/1945-7111/aba5d4.

[86] H. Becker, L. Castanheira, G. Hinds, Local measurement of current collector potential in a polymer electrolyte membrane water electrolyser, J. Power Sources. 448 (2020) 227563. doi:10.1016/j.jpowsour.2019.227563.

[87] Z. Kang, J. Mo, G. Yang, F.-Y. Zhang, S.T. Reterer, D.A. Cullen, Micro/Nano Manufacturing of Novel Multifunctional Layers for Hydrogen Production from Water Splitting, in: Proc. 12th IEEE Int. Conf. Nano/Micro Eng. Mol. Syst., Los Angeles, 2017: pp. 126–130.

[88] J. Lopata, Z. Kang, J. Young, G. Bender, J.W. Weidner, S. Shimpalee, Effects of the Transport/Catalyst Layer Interface and Catalyst Loading on Mass and Charge Transport Phenomena in Polymer Electrolyte Membrane Water Electrolysis Devices, J. Electrochem. Soc. 167 (2020) 064507. doi:10.1149/1945-7111/ab7f87.

[89] U. Babic, T.J. Schmidt, L. Gubler, Communication—Contribution of Catalyst Layer Proton Transport Resistance to Voltage Loss in Polymer Electrolyte Water Electrolyzers, J. Electrochem. Soc. 165 (2018) J3016–J3018. doi:10.1149/2.0031815jes.

[90] J.K. Lee, A. Bazylak, Optimizing Porous Transport Layer Design Parameters via Stochastic Pore Network Modelling : Reactant Transport and Interfacial Contact Considerations Optimizing Porous Transport Layer Design Parameters via Stochastic Pore Network Modelling : Reactant Tran, J. Electrochem. Soc. 167 (2020) 013541. doi:10.1149/1945-7111/ab6557.

[91] P. Millet, D. Dragoe, S. Grigoriev, V. Fateev, C. Etievant, GenHyPEM: A research program on PEM water electrolysis supported by the European Commission, Int. J. Hydrogen Energy. 34 (2009) 4974–4982. doi:10.1016/j.ijhydene.2008.11.114.

[92] P. Millet, R. Ngameni, S.A. Grigoriev, N. Mbemba, F. Brisset, A. Ranjbari, C. Etiévant, PEM water electrolyzers: From electrocatalysis to stack development, Int. J. Hydrogen Energy. 35 (2010) 5043–5052. doi:10.1016/j.ijhydene.2009.09.015.

[93] P. Millet, R. Ngameni, S.A. Grigoriev, V.N. Fateev, Scientific and engineering issues related to PEM technology: Water electrolysers, fuel cells and unitized regenerative systems, Int. J. Hydrogen Energy. 36 (2011) 4156–4163. doi:10.1016/j.ijhydene.2010.06.106.

[94] P. Millet, N. Mbemba, S.A. Grigoriev, V.N. Fateev, A. Aukauloo, C. Etiévant, Electrochemical performances of PEM water electrolysis cells and perspectives, Int. J. Hydrogen Energy. 36 (2011) 4134–4142. doi:10.1016/j.ijhydene.2010.06.105.

[95] S.A. Grigoriev, P. Millet, S.A. Volobuev, V.N. Fateev, Optimization of porous current collectors for PEM water electrolysers, Int. J. Hydrogen Energy. 34 (2009) 4968–4973. doi:10.1016/j.ijhydene.2008.11.056.

[96] J. Parra-Restrepo, R. Bligny, J. Dillet, S. Didierjean, D. Stemmelen, C. Moyne, A. Degiovanni, G. Maranzana, Influence of the porous transport layer properties on the mass and charge transfer in a segmented PEM electrolyzer, Int. J. Hydrogen Energy. 45 (2020) 8094–8106. doi:10.1016/j.ijhydene.2020.01.100.

[97] J. Mo, S.M. Steen III, S. Retterer, D.A. Cullen, A. Terekhov, F.-Y. Zhang, Mask-Patterned Wet Etching of Thin Titanium Liquid/Gas Diffusion Layers for a PEMEC, ECS Trans. 66 (2015) 3–10. doi:10.1149/06624.0003ecst.

[98] J. Mo, Z. Kang, G. Yang, S.T. Retterer, D.A. Cullen, T.J. Toops, J.B. Green, F.Y. Zhang, Thin liquid/gas diffusion layers for high-efficiency hydrogen production from water splitting, Appl.

Energy. 177 (2016) 817–822. doi:10.1016/j.apenergy.2016.05.154.

[99] Z. Kang, J. Mo, G. Yang, Y. Li, D.A. Talley, S.T. Retterer, D.A. Cullen, T.J. Toops, M.P. Brady, G. Bender, B.S. Pivovar, J.B. Green, F.-Y. Zhang, Thin film surface modifications of thin/tunable liquid/gas diffusion layers for high-efficiency proton exchange membrane electrolyzer cells, Appl. Energy. 206 (2017) 983–990. doi:10.1016/j.apenergy.2017.09.004.

[100] H. Li, T. Fujigaya, H. Nakajima, A. Inada, K. Ito, Optimum structural properties for an anode current collector used in a polymer electrolyte membrane water electrolyzer operated at the boiling point of water, J. Power Sources. 332 (2016) 16–23. doi:10.1016/j.jpowsour.2016.09.086.

[101] S.M. Steen, J. Mo, Z. Kang, G. Yang, F.Y. Zhang, Investigation of titanium liquid/gas diffusion layers in proton exchange membrane electrolyzer cells, Int. J. Green Energy. 14 (2017) 162–170. doi:10.1080/15435075.2016.1253582.

[102] N. Baumann, C. Cremers, K. Pinkwart, J. Tübke, Membrane Electrode Assemblies for Water Electrolysis using WO3-Supported IrxRu1-xO2Catalysts, Energy Technol. 4 (2016) 212–220. doi:10.1002/ente.201500258.

[103] U. Wittstadt, E. Wagner, T. Jungmann, Membrane electrode assemblies for unitised regenerative polymer electrolyte fuel cells, J. Power Sources. 145 (2005) 555–562. doi:10.1016/j.jpowsour.2005.02.068.

[104] S. Arisetty, A.K. Prasad, S.G. Advani, Metal foams as flow field and gas diffusion layer in direct methanol fuel cells, J. Power Sources. 165 (2007) 49–57. doi:10.1016/j.jpowsour.2006.12.008.

[105] A. Baroutaji, J.G. Carton, J. Stokes, A.G. Olabi, Application of Open Pore Cellular Foam for air breathing PEM fuel cell, Int. J. Hydrogen Energy. 42 (2017) 25630–25638. doi:10.1016/j.ijhydene.2017.05.114.

[106] P. Deevanhxay, T. Sasabe, S. Tsushima, S. Hirai, Effect of liquid water distribution in gas

diffusion media with and without microporous layer on PEM fuel cell performance, Electrochem. Commun. 34 (2013) 239–241. doi:10.1016/j.elecom.2013.07.001.

[107] M.S. Ismail, T. Damjanovic, D.B. Ingham, L. Ma, M. Pourkashanian, Effect of polytetrafluoroethylene-treatment and microporous layer-coating on the in-plane permeability of gas diffusion layers used in proton exchange membrane fuel cells, J. Power Sources. 195 (2010) 6619–6628. doi:10.1016/j.jpowsour.2010.04.036.

[108] C.J. Tseng, S.K. Lo, Effects of microstructure characteristics of gas diffusion layer and microporous layer on the performance of PEMFC, Energy Convers. Manag. 51 (2010) 677–684. doi:10.1016/j.enconman.2009.11.011.

[109] J.T. Gostick, M.A. Ioannidis, M.W. Fowler, M.D. Pritzker, On the role of the microporous layer in PEMFC operation, Electrochem. Commun. 11 (2009) 576–579. doi:10.1016/j.elecom.2008.12.053.

[110] U. Pasaogullari, C.Y. Wang, Two-phase transport and the role of micro-porous layer in polymer electrolyte fuel cells, Electrochim. Acta. 49 (2004) 4359–4369. doi:10.1016/j.electacta.2004.04.027.

[111] P. Lettenmeier, S. Kolb, F. Burggraf, A.S. Gago, K.A. Friedrich, Towards developing a backing layer for proton exchange membrane electrolyzers, J. Power Sources. 311 (2016) 153–158. doi:10.1016/j.jpowsour.2016.01.100.

[112] C.C. Sung, C.Y. Liu, A novel micro protective layer applied on a simplified PEM water electrolyser, Int. J. Hydrogen Energy. 38 (2013) 10063–10067. doi:10.1016/j.ijhydene.2013.06.034.

[113] C.Y. Liu, L.H. Hu, C.C. Sung, Micro-protective layer for lifetime extension of solid polymer electrolyte water electrolysis, J. Power Sources. 207 (2012) 81–85. doi:10.1016/j.jpowsour.2012.01.045.

[114] H. Ito, T. Maeda, A. Nakano, C.M. Hwang, M. Ishida, N. Yokoi, Y. Hasegawa, A. Kato, T. Yoshida, Influence of Different Gas Diffusion Layers on the Water Management of Polymer Electrolyte Unitized Reversible Fuel Cell, ECS Trans. 33 (2010) 945–954. doi:10.1149/1.3484588.

[115] C.M. Hwang, M. Ishida, H. Ito, T. Maeda, A. Nakano, Y. Hasegawa, N. Yokoi, A. Kato, T. Yoshida, Influence of properties of gas diffusion layers on the performance of polymer electrolyte-based unitized reversible fuel cells, Int. J. Hydrogen Energy. 36 (2011) 1740–1753. doi:10.1016/j.ijhydene.2010.10.091.

[116] C.M. Hwang, M. Ishida, H. Ito, T. Maeda, A. Nakano, A. Kato, T. Yoshida, Effect of titanium powder loading in gas diffusion layer of a polymer electrolyte unitized reversible fuel cell, J. Power Sources. 202 (2012) 108–113. doi:10.1016/j.jpowsour.2011.11.041.

[117] Z. Zhan, J. Xiao, D. Li, M. Pan, R. Yuan, Effects of porosity distribution variation on the liquid water flux through gas diffusion layers of PEM fuel cells, J. Power Sources. 160 (2006) 1041–1048. doi:10.1016/j.jpowsour.2006.02.060.

[118] Z. Zhan, J. Xiao, Y. Zhang, M. Pan, R. Yuan, Gas diffusion through differently structured gas diffusion layers of PEM fuel cells, Int. J. Hydrogen Energy. 32 (2007) 4443–4451. doi:10.1016/j.ijhydene.2007.03.041.

[119] Y. Zhang, A. Verma, R. Pitchumani, Optimum design of polymer electrolyte membrane fuel cell with graded porosity gas diffusion layer, Int. J. Hydrogen Energy. 41 (2016) 8412–8426. doi:10.1016/j.ijhydene.2016.02.077.

[120] P. Lettenmeier, S. Kolb, N. Sata, A. Fallisch, L. Zielke, S. Thiele, A.S. Gago, K.A. Friedrich, Comprehensive investigation of novel pore-graded gas diffusion layers for high-performance and cost-effective proton exchange membrane electrolyzers, Energy Environ. Sci. 10 (2017) 2521–2533. doi:10.1039/C7EE01240C.

[121] Z. Kang, S. Yu, G. Yang, Y. Li, G. Bender, B.S. Pivovar, J.B. Green, F.-Y. Zhang, Performance

improvement of proton exchange membrane electrolyzer cells by introducing in-plane transport enhancement layers, Electrochim. Acta. 316 (2019) 43–51. doi:10.1016/j.electacta.2019.05.096.

[122] A. Forner-Cuenca, J. Biesdorf, L. Gubler, P.M. Kristiansen, T.J. Schmidt, P. Boillat, Engineered Water Highways in Fuel Cells: Radiation Grafting of Gas Diffusion Layers, Adv. Mater. 27 (2015) 6317–6322. doi:10.1002/adma.201503557.

[123] A. Forner-Cuenca, V. Manzi-Orezzoli, J. Biesdorf, M. El Kazzi, D. Streich, L. Gubler, T.J. Schmidt, P. Boillat, Advanced Water Management in PEFCs: Diffusion Layers with Patterned Wettability: I. Synthetic Routes, Wettability Tuning and Thermal Stability, J. Electrochem. Soc. 163 (2016) F788–F801. doi:10.1149/2.0271608jes.

[124] A. Forner-Cuenca, J. Biesdorf, V. Manzi-Orezzoli, L. Gubler, T.J. Schmidt, P. Boillat, Advanced Water Management in PEFCs: Diffusion Layers with Patterned Wettability:II. Measurement of Capillary Pressure Characteristic with Neutron and Synchrotron Imaging, J. Electrochem. Soc. 163 (2016) F1389–F1398. doi:10.1149/2.0891613jes.

[125] A. Forner-Cuenca, J. Biesdorf, V. Manzi-Orezzoli, L. Gubler, T.J. Schmidt, P. Boillat, Advanced Water Management in PEFCs: Diffusion Layers with Patterned Wettability: III. Operando Characterization with Neutron Imaging, J. Electrochem. Soc. 163 (2016) F1389–F1398. doi:10.1149/2.0891613jes.

[126] A. Nouri-Khorasani, E. Tabu Ojong, T. Smolinka, D.P. Wilkinson, Model of oxygen bubbles and performance impact in the porous transport layer of PEM water electrolysis cells, Int. J. Hydrogen Energy. 42 (2017) 28665–28680. doi:10.1016/j.ijhydene.2017.09.167.

[127] Y. Li, Z. Kang, X. Deng, G. Yang, S. Yu, J. Mo, D.A. Talley, G.K. Jennings, F.Y. Zhang, Wettability effects of thin titanium liquid/gas diffusion layers in proton exchange membrane electrolyzer cells, Electrochim. Acta. 298 (2019) 704–708. doi:10.1016/j.electacta.2018.12.162.

[128] T. Bystron, M. Vesely, M. Paidar, G. Papakonstantinou, K. Sundmacher, B. Bensmann, R. Hanke-Rauschenbach, K. Bouzek, Enhancing PEM water electrolysis efficiency by reducing the extent of Ti gas diffusion layer passivation, J. Appl. Electrochem. 48 (2018) 713–723. doi:10.1007/s10800-018-1174-6.

[129] Z. Kang, S.M. Alia, J.L. Young, G. Bender, Effects of various parameters of different porous transport layers in proton exchange membrane water electrolysis, Electrochim. Acta. 354 (2020) 136641. doi:10.1016/j.electacta.2020.136641.

[130] M. Suermann, T. Gimpel, L. V. Bühre, W. Schade, B. Bensmann, R. Hanke-Rauschenbach, Femtosecond laser-induced surface structuring of the porous transport layers in proton exchange membrane water electrolysis, J. Mater. Chem. A. 8 (2020) 4898–4910. doi:10.1039/c9ta12127g.

[131] V.I. Kalikmanov, Nucleation Theory, 2013.

[132] Y. Li, Z. Kang, J. Mo, G. Yang, S. Yu, D.A. Talley, B. Han, F.Y. Zhang, In-situ investigation of bubble dynamics and two-phase flow in proton exchange membrane electrolyzer cells, Int. J. Hydrogen Energy. 43 (2018) 11223–11233. doi:10.1016/j.ijhydene.2018.05.006.

[133] A. Kusoglu, A.Z. Weber, New Insights into Perfluorinated Sulfonic-Acid Ionomers, Chem. Rev. 117 (2017) 987–1104. doi:10.1021/acs.chemrev.6b00159.

[134] P. Choi, N.H. Jalani, R. Datta, Thermodynamics and Proton Transport in Nafion, J. Electrochem. Soc. 152 (2005) E123. doi:10.1149/1.1859814.

[135] T.D. Gierke, G.E. Munn, F.C. Wilson, The Morphology in Nafion Perfluorinated Membrane Products, As Determined By Wide- and Small-Angle X-Ray Studies., J. Polym. Sci. Part A-2, Polym. Phys. 19 (1981) 1687–1704. doi:10.1002/pol.1981.180191103.

[136] W.Y. Hsu, T.D. Gierke, T.D. Gierke, Elastic Theory for Ionic Clustering in Perfluorinated Ionomers, Macromolecules. 15 (1982) 101–105. doi:10.1021/ma00229a020.

[137] M. Fujimura, T. Hashimoto, H. Hawai, Small-Angle X-ray Scattering Study of Perfluorinated Ionomer Membranes. 1. Origin of Two Scattering Maxima, Macromolecules. 14 (1981) 1309–1315. doi:10.1021/ma50006a032.

[138] M. Fujimura, T. Hashimoto, H. Kawai, Small-Angle X-ray Scattering Study of Perfluorinated Ionomer Membranes. 2. Models for Ionic Scattering Maximum, Macromolecules. 15 (1982) 136–144. doi:10.1021/ma00229a028.

[139] K. Schmidt-Rohr, Q. Chen, Parallel cylindrical water nanochannels in Nafion fuel-cell membranes, Nat. Mater. 7 (2008) 75–83. doi:10.1038/nmat2074.

[140] L. Rubatat, G. Gebel, O. Diat, Fibrillar structure of Nafion: Matching fourier and real space studies of corresponding films and solutions, Macromolecules. 37 (2004) 7772–7783. doi:10.1021/ma049683j.

[141] H.W. Starkweather, Crystallinity in Perfluorosulfonic Acid Ionomers and Related Polymers, Macromolecules. 15 (1982) 320–323. doi:10.1021/ma00230a023.

[142] H.G. Haubold, T. Vad, H. Jungbluth, P. Hiller, Nano structure of NAFION: A SAXS study, Electrochim. Acta. 46 (2001) 1559–1563. doi:10.1016/S0013-4686(00)00753-2.

[143] K.D. Kreuer, G. Portale, A critical revision of the nano-morphology of proton conducting ionomers and polyelectrolytes for fuel cell applications, Adv. Funct. Mater. 23 (2013) 5390–5397. doi:10.1002/adfm.201300376.

[144] A. Kusoglu, M.A. Modestino, A. Hexemer, R.A. Segalman, A.Z. Weber, Subsecond morphological changes in nafion during water uptake detected by small-angle X-ray scattering, ACS Macro Lett. 1 (2012) 33–36. doi:10.1021/mz200015c.

[145] M. Litt, A reevaluation of Nafion (R) morphology, Polym. Prepr. 38 (1997) 80–81.

[146] L. Rubatat, A.L. Rollet, G. Gebel, O. Diat, Evidence of elongated polymeric aggregates in Nafion, Macromolecules. 35 (2002) 4050–4055. doi:10.1021/ma011578b.

[147] M. Fumagalli, S. Lyonnard, G. Prajapati, Q. Berrod, L. Porcar, A. Guillermo, G. Gebel, Fast Water Diffusion and Long-Term Polymer Reorganization during Nafion Membrane Hydration Evidenced by Time-Resolved Small-Angle Neutron Scattering, J. Phys. Chem. B. 119 (2015) 7068–7076. doi:10.1021/acs.jpcb.5b01220.

[148] G. Gebel, Structural evolution of water swollen perfluorosulfonated ionomers from dry membrane to solution, Polymer (Guildf). 41 (2000) 5829–5838. doi:10.1016/S0032-3861(99)00770-3.

[149] S. Kumar, M. Pineri, Interpretation of small-angle x-ray and neutron scattering data for perfluorosulfonated ionomer membranes, J. Polym. Sci. Part B Polym. Phys. 24 (1986) 1767–1782. doi:10.1002/polb.1986.090240812.

[150] T.A. Zawodzinski, M. Neeman, L.O. Sillerud, S. Gottesfeld, Determination of water diffusion coefficients in perfluorosulfonate ionomeric membranes, J. Phys. Chem. 95 (1991) 6040–6044. doi:10.1021/j100168a060.

[151] M. Falk, An infrared study of water in perfluorosulfonate (Nafion) membranes, Can. J. Chem. 58 (1980) 1495–1501. doi:10.1139/v80-237.

[152] N.G. Boyle, V.J. McBrierty, A. Eisenberg, Nmr Investigation of Molecular Motion in Nation Membranes, Macromolecules. 16 (1983) 80–84. doi:10.1021/ma00235a016.

[153] S.J. Paddison, T.A. Zawodzinski, Molecular modeling of the pendant chain in Nafion®, Solid State Ionics. 113–115 (1998) 333–340. doi:10.1016/s0167-2738(98)00298-7.

[154] A. Bocarsly, D.M.P. Mingos, Fuel Cells and Hydrogen Storage, 2011. doi:10.1007/978-3-642-21780-7.

[155] Q. Zhao, P. Majsztrik, J. Benziger, Diffusion and interfacial transport of water in Nafion, J. Phys. Chem. B. 115 (2011) 2717–2727. doi:10.1021/jp1112125.

[156] P. Medina, M. Santarelli, Analysis of water transport in a high pressure PEM electrolyzer, Int. J.

Hydrogen Energy. 35 (2010) 5173–5186. doi:10.1016/j.ijhydene.2010.02.130.

[157] S.A. Fischer, B.I. Dunlap, D. Gunlycke, Correlated dynamics in aqueous proton diffusion, Chem. Sci. 9 (2018) 7126–7132. doi:10.1039/c8sc01253a.

[158] N. Agmon, The Grotthuss mechanism, Chem. Phys. Lett. 244 (1995) 456–462. doi:10.1016/0009-2614(95)00905-J.

[159] L. Liu, W. Chen, Y. Li, An overview of the proton conductivity of nafion membranes through a statistical analysis, J. Memb. Sci. 504 (2016) 1–9. doi:10.1016/j.memsci.2015.12.065.

[160] K.D. Kreuer, Proton conductivity: Materials and applications, Chem. Mater. 8 (1996) 610–641. doi:10.1021/cm950192a.

[161] H. Sun, M. Yu, Z. Li, S. Almheiri, A molecular dynamic simulation of hydrated proton transfer in perfluorosulfonate ionomer membranes (Nafion 117), J. Chem. 2015 (2015). doi:10.1155/2015/169680.

[162] P. Choi, N.H. Jalani, R. Datta, Thermodynamics and proton transport in Nafion II. Proton diffusion mechanisms and conductivity, J. Electrochem. Soc. 152 (2005). doi:10.1149/1.1859814.

[163] R. Paul, S.J. Paddison, The phenomena of dielectric saturation in the water domains of polymer electrolyte membranes, Solid State Ionics. 168 (2004) 245–248. doi:10.1016/j.ssi.2003.06.001.

[164] M. Eikerling, A.A. Kornyshev, A.M. Kuznetsov, J. Ulstrup, S. Walbran, Mechanisms of proton conductance in polymer electrolyte membranes, J. Phys. Chem. B. 105 (2002) 3646–3662. doi:10.1021/jp003182s.

[165] Y.K. Choe, E. Tsuchida, T. Ikeshoji, S. Yamakawa, S.A. Hyodo, Nature of proton dynamics in a polymer electrolyte membrane, nafion: A first-principles molecular dynamics study, Phys. Chem. Chem. Phys. 11 (2009) 3892–3899. doi:10.1039/b819535h.

[166] T. Schuler, T.J. Schmidt, F.N. Büchi, Polymer Electrolyte Water Electrolysis: Correlating

Performance and Porous Transport Layer Structure: Part II. Electrochemical Performance Analysis, J. Electrochem. Soc. 166 (2019) F555–F565. doi:10.1149/2.1241908jes.

[167] J.O. Majasan, F. Iacoviello, J.I.S. Cho, M. Maier, X. Lu, T.P. Neville, I. Dedigama, P.R. Shearing, D.J.L. Brett, Correlative study of microstructure and performance for porous transport layers in polymer electrolyte membrane water electrolysers by X-ray computed tomography and electrochemical characterization, Int. J. Hydrogen Energy. 44 (2019) 19519–19532. doi:10.1016/j.ijhydene.2019.05.222.

[168] O.F. Selamet, U. Pasaogullari, D. Spernjak, D.S. Hussey, D.L. Jacobsen, M.D. Mat, In-situ two-phase flow investigation of Proton Exchange Membrane (PEM) electrolyzer by simultaneous optical and neutron imaging, ECS Trans. 41 (2011) 349–362.

[169] O. Panchenko, L. Giesenberg, E. Borgardt, W. Zwaygardt, N. Kardjilov, H. Markötter, T. Arlt, I. Manke, M. Müller, D. Stolten, W. Lehnert, Influence of Stoichiometry on the Two-Phase Flow Behavior of Proton Exchange Membrane Electrolyzers, Energies. 12 (2019) 350. doi:10.3390/en12030350.

[170] C.H. Lee, J.K. Lee, M.G. George, K.F. Fahy, J.M. LaManna, E. Baltic, D.S. Hussey, D.L. Jacobson, A. Bazylak, Reconciling temperature-dependent factors affecting mass transport losses in polymer electrolyte membrane electrolyzers, Energy Convers. Manag. 213 (2020) 112797. doi:10.1016/j.enconman.2020.112797.

[171] E. Leonard, A.D. Shum, N. Danilovic, C. Capuano, K.E. Ayers, L.M. Pant, A.Z. Weber, X. Xiao, D.Y. Parkinson, I. V. Zenyuk, Interfacial analysis of a PEM electrolyzer using X-ray computed tomography, Sustain. Energy Fuels. 4 (2020) 921–931. doi:10.1039/c9se00364a.

[172] L. Zielke, A. Fallisch, N. Paust, R. Zengerle, S. Thiele, Tomography based screening of flow field / current collector combinations for PEM water electrolysis, RSC Adv. 4 (2014) 58888–58894. doi:10.1039/C4RA12402B.

[173] C. Lee, J.K. Lee, B. Zhao, K.F. Fahy, A. Bazylak, Transient Gas Distribution in Porous Transport Layers of Polymer Electrolyte Membrane Electrolyzers, J. Electrochem. Soc. 167 (2020) 024508. doi:10.1149/1945-7111/ab68c8.

[174] U. Panchenko, T. Arlt, I. Manke, M. Müller, D. Stolten, W. Lehnert, Synchrotron Radiography for a Proton Exchange Membrane (PEM) Electrolyzer, Fuel Cells. (2020) 1–7. doi:10.1002/fuce.201900055.

[175] F. Arbabi, A. Kalantarian, R. Abouatallah, R. Wang, J.S. Wallace, A. Bazylak, Feasibility study of using microfluidic platforms for visualizing bubble flows in electrolyzer gas diffusion layers, J. Power Sources. 258 (2014) 142–149. doi:10.1016/j.jpowsour.2014.02.042.

[176] C.H. Lee, J. Hinebaugh, R. Banerjee, S. Chevalier, R. Abouatallah, R. Wang, A. Bazylak, Influence of limiting throat and flow regime on oxygen bubble saturation of polymer electrolyte membrane electrolyzer porous transport layers, Int. J. Hydrogen Energy. 42 (2017) 2724–2735. doi:10.1016/j.ijhydene.2016.09.114.

[177] M. Maier, Q. Meyer, J. Majasan, R.E. Owen, J.B. Robinson, J. Dodwell, Y. Wu, L. Castanheira, G. Hinds, P.R. Shearing, D.J.L. Brett, Diagnosing Stagnant Gas Bubbles in a Polymer Electrolyte Membrane Water Electrolyser Using Acoustic Emission, Front. Energy Res. 8 (2020). doi:10.3389/fenrg.2020.582919.

[178] M. Maier, R.E. Owen, M.T.M. Pham, J. Dodwell, J. Majasan, J.B. Robinson, G. Hinds, P.R. Shearing, D.J.L. Brett, Acoustic time-of-flight imaging of polymer electrolyte membrane water electrolysers to probe internal structure and flow characteristics, Int. J. Hydrogen Energy. 46 (2021) 11523–11535. doi:10.1016/j.ijhydene.2021.01.077.

[179] J.C. Garcia-Navarro, M. Schulze, K.A. Friedrich, Measuring and modeling mass transport losses in proton exchange membrane water electrolyzers using electrochemical impedance spectroscopy, J. Power Sources. 431 (2019) 189–204. doi:10.1016/j.jpowsour.2019.05.027.

[180] P. Lettenmeier, R. Wang, R. Abouatallah, S. Helmly, T. Morawietz, R. Hiesgen, S. Kolb, F. Burggraf, J. Kallo, A.S. Gago, K.A. Friedrich, Durable Membrane Electrode Assemblies for Proton Exchange Membrane Electrolyzer Systems Operating at High Current Densities, Electrochim. Acta. 210 (2016) 502–511. doi:10.1016/j.electacta.2016.04.164.

[181] C. Rozain, P. Millet, Electrochemical characterization of Polymer Electrolyte Membrane Water Electrolysis Cells, Electrochim. Acta. 131 (2014) 160–167. doi:10.1016/j.electacta.2014.01.099.

[182] S. Siracusano, S. Trocino, N. Briguglio, V. Baglio, A.S. Aricò, Electrochemical impedance spectroscopy as a diagnostic tool in polymer electrolyte membrane electrolysis, Materials (Basel). 11 (2018). doi:10.3390/ma11081368.

[183] E. Ivers-Tiffee, A. Weber, Evaluation of electrochemical impedance spectra by the distribution of relaxation times, J. Ceram. Soc. Japan. 125 (2017) 193–201. doi:10.2109/jcersj2.16267.

[184] J. Illig, M. Ender, T. Chrobak, J.P. Schmidt, D. Klotz, E. Ivers-Tiffée, Separation of charge transfer and contact resistance in LiFePO 4-Cathodes by impedance Modeling, J. Electrochem. Soc. 159 (2012) 952–960. doi:10.1149/2.030207jes.

[185] H. Schichlein, A.C. Müller, M. Voigts, A. Krügel, E. Ivers-Tiffée, Deconvolution of electrochemical impedance spectra for the identification of electrode reaction mechanisms in solid oxide fuel cells, J. Appl. Electrochem. 32 (2002) 875–882. doi:10.1023/A:1020599525160.

[186] X.-Z. Yuan, C. Song, H. Wang, J. Zhang, Electrochemical Impedance Spectroscopy in PEM Fuel Cells: Fundamentals and Applications, Springer Verlag, London, 2010. doi:10.1007/978-1-84882-846-9.

[187] M. Bernt, A. Siebel, H.A. Gasteiger, Analysis of Voltage Losses in PEM Water Electrolyzers with Low Platinum Group Metal Loadings, J. Electrochem. Soc. 165 (2018) F305–F314. doi:10.1149/2.0641805jes.

[188] J.O. Majasan, F. Iacoviello, P.R. Shearing, D.J. Brett, Effect of Microstructure of Porous

Transport Layer on Performance in Polymer Electrolyte Membrane Water Electrolyser, Energy Procedia. 151 (2018) 111–119. doi:10.1016/j.egypro.2018.09.035.

[189] A. Weiß, A. Siebel, M. Bernt, T.-H. Shen, V. Tileli, H.A. Gasteiger, Impact of Intermittent Operation on Lifetime and Performance of a PEM Water Electrolyzer, J. Electrochem. Soc. 166 (2019) F487–F497. doi:10.1149/2.0421908jes.

[190] M. Suermann, K. Takanohashi, A. Lamibrac, T.J. Schmidt, F.N. Büchi, Influence of Operating Conditions and Material Properties on the Mass Transport Losses of Polymer Electrolyte Water Electrolysis, J. Electrochem. Soc. 164 (2017) F973–F980. doi:10.1149/2.13517109jes.

[191] T. Schuler, R. De Bruycker, T.J. Schmidt, F.N. Büchi, Polymer Electrolyte Water Electrolysis: Correlating Porous Transport Layer Structural Properties and Performance: Part I. Tomographic Analysis of Morphology and Topology, J. Electrochem. Soc. 166 (2019) F270–F281. doi:10.1149/2.0561904jes.

[192] Y. Li, G. Yang, S. Yu, Z. Kang, D.A. Talley, F.Y. Zhang, Direct thermal visualization of micro-scale hydrogen evolution reactions in proton exchange membrane electrolyzer cells, Energy Convers. Manag. 199 (2019) 111935. doi:10.1016/j.enconman.2019.111935.

[193] Z. Kang, J. Mo, G. Yang, Y. Li, D.A. Talley, B. Han, F.Y. Zhang, Performance Modeling and Current Mapping of Proton Exchange Membrane Electrolyzer Cells with Novel Thin/Tunable Liquid/Gas Diffusion Layers, Electrochim. Acta. 255 (2017) 405–416. doi:10.1016/j.electacta.2017.09.170.

[194] S.S. Lafmejani, A.C. Olesen, S.K. Kaer, Analysing Gas-Liquid Flow in PEM Electrolyser Micro-Channels, ECS Trans. 75 (2016) 1121–1127.

[195] H. Altaf, N. Vorhauer, E. Tsotsas, T. Vidaković-Koch, Steady-State Water Drainage by Oxygen in Anodic Porous Transport Layer of Electrolyzers: A 2D Pore Network Study, Processes. 8 (2020) 362. doi:10.3390/pr8030362.